The Astrophysical Journal Supplement Series, 239:8 (25pp), 2018 November https://doi.org/10.3847/1538-4365/aae436

The EBEX Balloon-borne Experiment—Detectors and Readout

The EBEX Collaboration,
Maximilian Abitbol[1], Asad M. Aboobaker[2,3,18], Peter Ade[4], Derek Araujo[1], François Aubin[2,5,18], Carlo Baccigalupi[6,7], Chaoyun Bao[2], Daniel Chapman[1], Joy Didier[1,8,18], Matt Dobbs[5,9], Stephen M. Feeney[10,11,18], Christopher Geach[2], Will Grainger[4], Shaul Hanany[2], Kyle Helson[12,13,18], Seth Hillbrand[1], Gene Hilton[14], Johannes Hubmayr[14], Kent Irwin[14,15,18], Andrew Jaffe[10], Bradley Johnson[1], Terry Jones[2], Jeff Klein[2], Andrei Korotkov[12], Adrian Lee[16], Lorne Levinson[17], Michele Limon[1], Kevin MacDermid[5], Amber D. Miller[1,8,18], Michael Milligan[2], Kate Raach[2], Britt Reichborn-Kjennerud[1], Carl Reintsema[14], Ilan Sagiv[17], Graeme Smecher[5], Gregory S. Tucker[12], Benjamin Westbrook[16], Karl Young[2], and Kyle Zilic[2]
[1] Physics Department, Columbia University, New York, NY 10027, USA
[2] School of Physics and Astronomy, University of Minnesota–Twin Cities, Minneapolis, MN 55455, USA; faubin@umn.edu
[3] Jet Propulsion Laboratory, California Institute of Technology, Pasadena, CA 91109, USA
[4] Rutherford Appleton Lab, Harwell Oxford, OX11 0QX, UK
[5] Department of Physics, McGill University, Montreal, H3A 2T8, Canada
[6] Astrophysics Sector, SISSA, Trieste, I-34014, Italy
[7] INFN, Sezione di Trieste, Via Valerio 2, I-34127 Trieste, Italy
[8] Department of Physics and Astronomy, University of Southern California, Los Angeles, CA 90089, USA
[9] Canadian Institute for Advanced Research, Toronto, ON M5G 1Z8, Canada
[10] Department of Physics, Imperial College, London, SW7 2AZ, UK
[11] Center for Computational Astrophysics, Flatiron Institute, New York, NY 10010, USA
[12] Department of Physics, Brown University, Providence, RI 02912, USA
[13] NASA Goddard Space Flight Center, Greenbelt, MD 20771, USA
[14] National Institute of Standards and Technology, Boulder, CO 80305, USA
[15] Department of Physics, Stanford University, Stanford, CA 94305, USA
[16] Department of Physics, University of California, Berkeley, CA 94720, USA
[17] Faculty of Physics, Weizmann Institute of Science, Rehovot, 76100, Israel
Received 2018 March 1; revised 2018 September 15; accepted 2018 September 18; published 2018 November 6

Abstract

EBEX was a long-duration balloon-borne experiment to measure the polarization of the cosmic microwave background. The experiment had three frequency bands centered at 150, 250, and 410 GHz and was the first to use a kilopixel array of transition edge sensor bolometers aboard a balloon platform. We describe the design and characterization of the array and the readout system. From the lowest to highest frequency, the median measured detectors' average thermal conductances were 39, 53, and 63 pW/K, the medians of transition temperatures were 0.45, 0.48, and 0.47 K, and the medians of normal resistances were 1.9, 1.5, and 1.4 Ω; we also give the measured distributions. With the exception of the thermal conductance at 150 GHz, all measured values are within 30% of their design. We measure median low-loop-gain time constants $\tau_0 = 88$, 46, and 57 ms. Two measurements of bolometer absorption efficiency gave results consistent within 10% and showing high (∼0.9) efficiency at 150 GHz and medium (∼0.35 and ∼0.25) efficiency at the two higher bands. We measure a median total optical power absorbed of 3.6, 5.3, and 5.0 pW. EBEX pioneered the use of the digital version of the frequency domain multiplexing system. We multiplexed the bias and readout of 16 bolometers onto two wires. The median per-detector noise-equivalent temperatures are 400, 920, and 14,500 $\mu K_{cmb}\sqrt{s}$. We compare these values to our preflight predictions and to a previous balloon payload. We discuss the sources of excess noise and the path for a future payload to make full use of the balloon environment.

Key words: balloons – cosmic background radiation – cosmology: observations – instrumentation: detectors – instrumentation: polarimeters

1. Introduction

Measurements of the cosmic microwave background (CMB) have provided a wealth of information about the physical mechanisms responsible for the evolution of the universe. In recent years, experimental efforts have focused on measuring the CMB's polarization patterns: *E*-modes and *B*-modes (Zaldarriaga & Seljak 1997). The level and specific shape of the angular power spectrum of CMB *E*-mode polarization can be predicted given the measured intensity anisotropy. Lensing of *E*-modes by the large-scale structure of the universe produces cosmological *B*-modes at small angular scales. An inflationary phase at sufficiently high energy scales near the big bang is predicted to leave another perhaps detectable *B*-mode signature at large and intermediate angular scales (Baumann et al. 2009).

The *E*-mode polarization of the CMB was first detected by the DASI experiment (Kovac et al. 2002), and other experiments soon followed suit (Scott & Smoot 2010). The combination of all measurements is in excellent agreement with predictions. *B*-mode polarization from gravitational lensing of *E*-modes and from Galactic dust emission has also recently been detected (Hanson et al. 2013; Ade et al. 2014;

[18] Current affiliation.

BICEP2 Collaboration et al. 2014; Naess et al. 2014; BICEP2/Keck & Planck Collaborations et al. 2015). Intense efforts are ongoing by ground- and balloon-based instruments to improve the measurements, separate the Galactic from the cosmological signals, and identify the inflationary B-mode signature.

The E and B Experiment (EBEX) was a balloon-borne CMB polarimeter designed to detect or constrain the levels of the inflationary gravitational wave and lensing B-mode power spectra. EBEX was also designed to be a technology pathfinder for future CMB space missions. To achieve instrument sensitivity, we implemented a kilopixel array of transition edge sensor (TES) bolometers and planned for a long-duration balloon flight. We included three spectral bands centered on 150, 250, and 410 GHz to give sensitivity to both the CMB and the Galactic dust foreground. The combination of the 400 deg^2 intended survey size and an optical system with $0.^\circ1$ resolution gave sensitivity to the range $30 < \ell < 1500$ of the angular power spectrum. Polarimetry was achieved with a continuously rotating achromatic half-wave plate (HWP) and a wire grid analyzer.

Design and construction of the experiment began in 2005. A 10 hr engineering flight was launched from Ft. Sumner, NM, on 2009 June 11, and the long-duration science flight was launched from McMurdo Station, Antarctica, on 2012 December 29. Data collection ceased when cryogens expired after 11 days, as planned. Because the majority of the flight occurred during 2013 January, we refer to this flight as EBEX2013.

This paper is one of a series of papers describing the experiment and its in-flight performance. This paper, called EBEX Paper 2, discusses the detectors and readout; EBEX Paper 1 (EP1; The EBEX Collaboration 2018a) describes the optical system, the receiver, and the polarimetric approach; EBEX Paper 3 (EP3; The EBEX Collaboration 2018b) gives information about the gondola, the attitude control system, and other support systems. A fourth paper, EBEX Paper 4 (EP4; Didier et al. 2017), discusses effects associated with detector nonlinearity and their influence on polarimetric measurements. Several other publications give additional details about EBEX. Some are from earlier stages of the program (Oxley et al. 2004; Grainger et al. 2008; Hubmayr et al. 2008; Aubin et al. 2010; Milligan et al. 2010; Reichborn-Kjennerud et al. 2010; Klein et al. 2011; Sagiv et al. 2012; Westbrook et al. 2012), and others discuss some subsystems in more detail (Polsgrove 2009; Reichborn-Kjennerud 2010; Sagiv 2011; Aubin 2012; MacDermid 2014; MacDermid et al. 2014; Westbrook 2014; Zilic 2014; Chapman et al. 2014, 2015; Chapman 2015; Didier et al. 2015; Didier 2016; Aubin et al. 2017).

Several new technologies have been implemented and tested for the first time in the EBEX instrument. It was the first astrophysical instrument to implement and operate a superconducting magnetic bearing (SMB), which was used to levitate the HWP. This system was discussed in EP1. EBEX was also the first balloon-borne experiment to implement a kilopixel array of TES bolometric detectors and the first experiment to implement a digital frequency domain multiplexing (FDM) system to read out the TES arrays. The implementation of these new technologies aboard a balloon flight presented several new challenges. These included the development of detectors that were optimized for the smaller optical loading at the stratosphere and that were tuned to operate at higher-frequency bands compared to those typically used on ground-based instruments and the development of a readout system with as low power dissipation per channel as realistically implementable while still giving low noise and a low $1/f$ knee.

This paper describes our implementation of the readout system and the design and characterization of the bolometers. In Section 2 we give a brief overview of the instrument, its optical system, and the design of the focal plane. Section 3 gives the characteristics of the time-domain data and describes the processing that was necessary to extract time-domain noise levels. The implementation of the readout system and an assessment of its noise and gain stability are the subject of Section 4. In Section 5 we discuss the design of the detectors and give results from laboratory characterization measurements. We also describe the measured in-flight radiative load and use this measurement as one of three approaches to extract the bolometer absorption efficiencies. We end this section with a discussion of the measured noise-equivalent power (NEP). In Section 6 we report our measurements of the noise-equivalent temperature (NET) and the final map depth at each of the three frequency bands. We discuss and summarize our findings in Section 7.

2. The EBEX Instrument and Focal Planes

The EBEX optical system consisted of a 105 cm aperture off-axis Gregorian telescope coupled to a cryogenic receiver containing refractive optics, a rotating achromatic HWP at a cold aperture stop, and a polarizing grid that directed independent polarizations to each of two focal planes cooled to a bath temperature of $\sim$0.25 K; see Figure 1. The focal planes were referred to as the H (horizontal) and V (vertical) focal planes. The optical and cryogenic systems are described in detail in EP1.

Figure 2 shows the elements of a focal plane. It consisted of a layer of electromagnetic filters, a monolithic array of feed horns attached to a monolithic array of waveguides, seven detector wafers coupled to wafer holders and inductor and capacitor (LC) boards, and a back cover. The back cover, together with the array of horns, completed a Faraday cage around the focal plane. The electromagnetic filters and waveguides defined frequency bands centered on 150, 250, and 410 GHz. Each focal plane was arranged such that four wafers operated at 150 GHz, two at 250 GHz, and one at 410 GHz; see Figure 2. The LC boards were part of the multiplexed frequency domain bias and readout of the detectors; see Section 4. Each detector wafer had 140 lithographically fabricated bolometers, of which up to 127 could be biased and read out with eight pairs of wires; see Section 5.2.

Each TES bolometer had a pair of electrical lines lithographed with niobium connected to bond pads at the edge of its wafer. Wire bonds connected the wafer to an LC board, which contained inductors and capacitors that were part of the FDM readout; see Section 4. We placed each silicon wafer onto a wafer-shaped piece of Invar thinly coated with warmed Apiezon N grease. For the edge wafers, the Invar was screwed into an aluminum mount holding the LC board in the same plane as the wafers. For the central wafer, we mounted the LC board below this plane with standoffs. To align the wafers with the feed horns, we doweled the wafer's aluminum mount to a jig that simulated the waveguide array

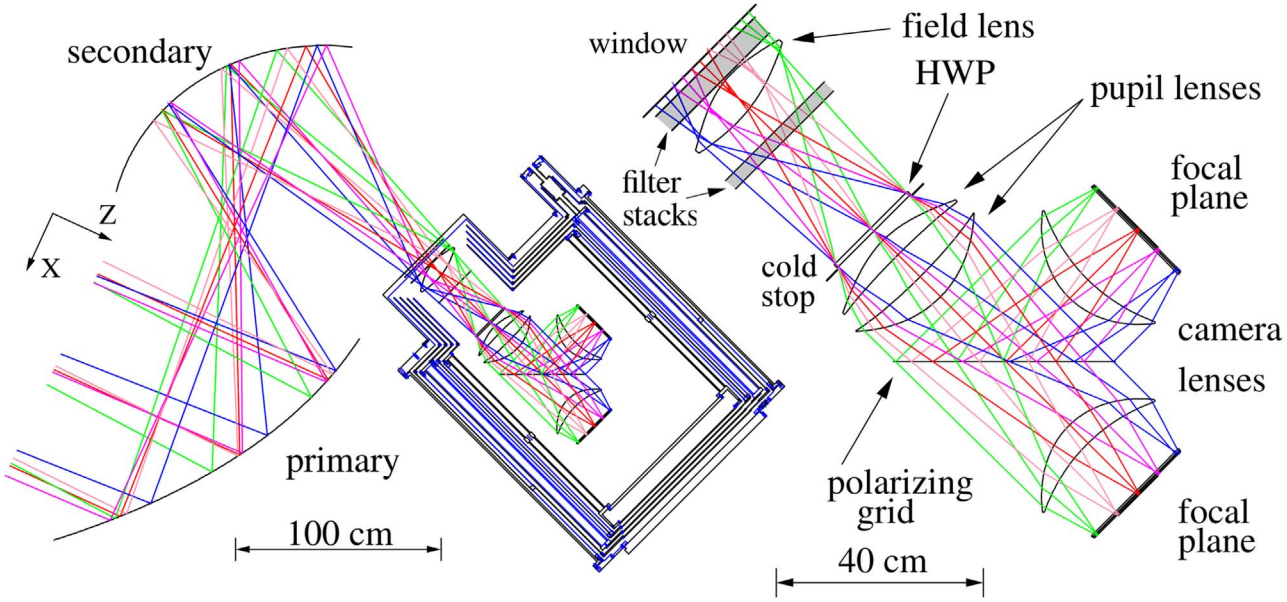

Figure 1. Left: ray-tracing of the EBEX optical design consisting of two ambient temperature reflectors in a Gregorian configuration and a cryogenic receiver. Right: inside the receiver, cryogenically cooled polyethylene lenses formed a cold stop and provided diffraction-limited performance over a flat, telecentric, 6.°6 field of view. Two identical focal planes (H and V) terminated the optical path.

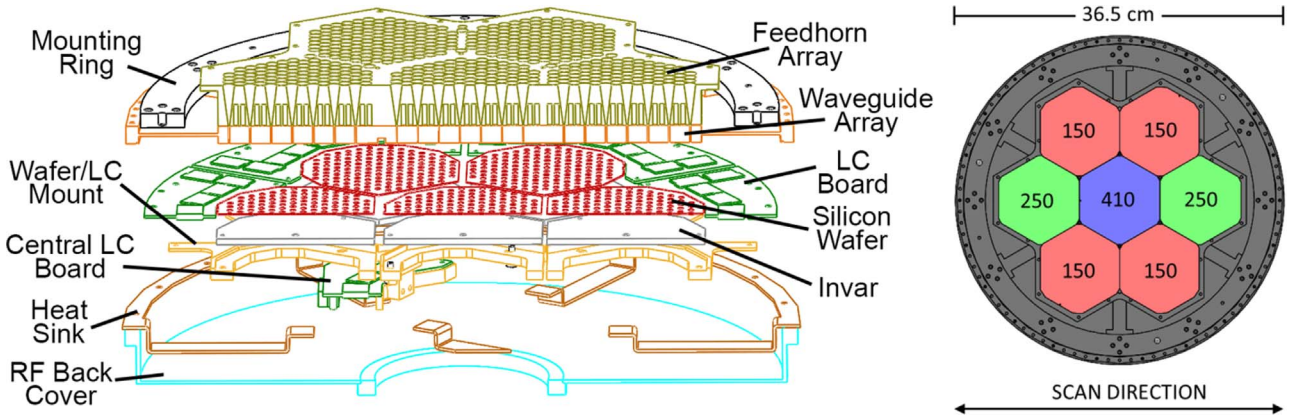

Figure 2. Left: solid model cross section through one of the EBEX focal planes. Right: sketch of a photon view. The instrument had two identical focal planes. The colors of the hexagons (and numbers) encode frequency bands (in GHz).

but had fewer, larger holes. We warmed the Invar and nudged the wafers until the bolometers were aligned with the alignment holes. The same alignment dowels that were used with the jig were later used with the waveguide and feed horn array. We soldered to the LC boards a commercially made microstrip with copper traces that was terminated with a micro-D connector. An additional set of self-made microstrips with niobium wires, which are described in Section 4.1, transmitted the signals to the superconducting quantum interference device (SQUID) boards. Commercial wire harnesses with manganin twisted pairs embedded in a Nomex weave connected the SQUID boards to the room-temperature readout electronics.

3. The Time-domain Data

During polarimetric observations, we rotated the HWP at $f_{\rm HWP} = 1.235$ Hz. This frequency was chosen considering the intended sky scan speed and the preflight measured detector time constants. The combination of the HWP rotation and the fixed polarizing grid modulated the polarized radiation incident on the HWP at frequency $4f_{\rm HWP}$ in the bolometer time-ordered data (TOD). Sources of incident polarized radiation included polarized sky sources, such as the Galaxy and the CMB, polarized emission by the instrument, primarily arising from the two reflectors, and sources of instrumental polarization. As described in EP1, the primary source of instrumental polarization was the field lens, but there were also smaller contributions from the reflectors and the vacuum window. The instrument polarized emissions and instrumental polarization were much more intense than both polarized sky emissions and instrument noise. Figure 3 shows the typical characteristics of the calibrated TOD during a period in which the HWP was rotating. A large-amplitude signal that is synchronous with the rotation of the HWP, and which we call half-wave plate synchronous signal (HWPSS), is apparent at harmonics of the HWP rotation frequency and is due to the mostly time-stable instrumental polarization and instrumental polarized emission. The spectral density of the TOD, also given in Figure 3, shows that the amplitude of the HWPSS is orders of

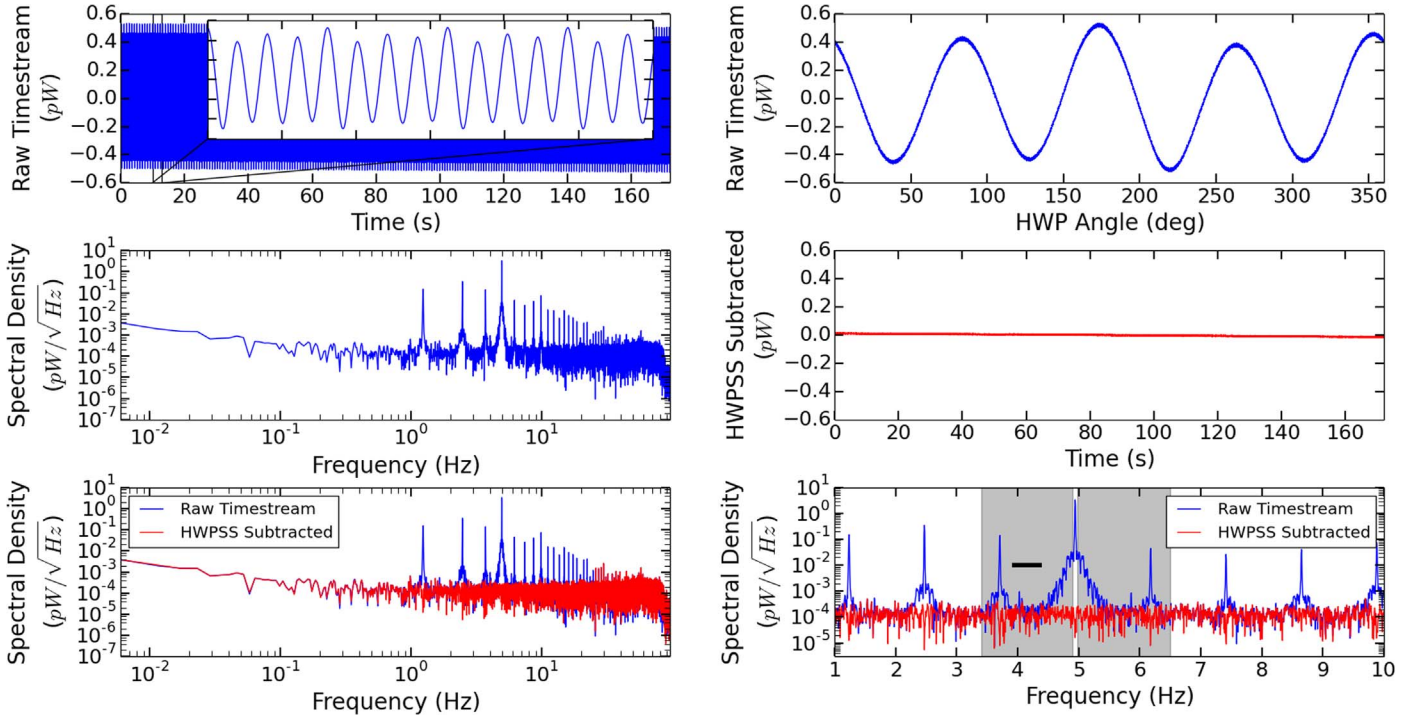

Figure 3. Time-ordered and spectral density data for a 172 s section of a 150 GHz detector before (blue) and after (red) HWPSS removal. The TOD are given in units of power incident on the telescope. For the 150 GHz band, 0.31 pW power fluctuation is equivalent to 1 $K_{\rm CMB}$. Top left: calibrated time-domain data and a magnified view of 3 s (inset) showing a sinusoidal behavior in time. Top right: data in HWP angle demonstrating a stable signal that is synchronous with the rotation of the HWP. Middle left: spectral density of the data. Middle right: data (top left) after subtraction of the HWPSS. Bottom left: spectral densities before and after HWPSS removal. Bottom right: spectral densities before and after HWPSS removal on a linear frequency scale, showing the first eight harmonics of the HWP rotation frequency. The shaded region indicates the sidebands surrounding the fourth harmonic, in which the Q and U signals reside. The black bar indicates the frequency range (from 3.9 to 4.4 Hz) used to quantify noise levels.

magnitude larger than the white-noise level. The maximum Galactic signal at 150 GHz is expected to be 0.3 fW, also much smaller than the HWPSS. Didier (2016), Araujo (2017), and Didier et al. (2017) give more information about the HWPSS.

In this paper we give an assessment of the noise properties of the instrument, including during astrophysical observations. To assess these noise properties, we first removed the HWPSS. The HWPSS is modeled as the sum of the first 20 harmonics of the HWP rotation frequency. The HWPSS for a given detector is estimated by performing a maximum likelihood fit of the sine and cosine amplitudes of the harmonics on 60 s chunks of data. In addition to a constant term, the amplitudes are also allowed to vary linearly with time. This procedure follows the one used for MAXIPOL (Johnson et al. 2007), and more details are given in Didier (2016) and in Araujo (2017). The HWPSS is subtracted from the raw detector time stream to yield the "HWPSS-subtracted" time stream. When we quote noise properties, we give special attention to a narrow band of frequencies between 3.9 and 4.4 Hz. This band is within the sideband of the fourth harmonic of the HWP rotation, which contains half of the Stokes Q and U sky synchronous signals. (The other half is contained in a symmetric sideband placed above the fourth harmonic, and we find the noise level there to be essentially identical to the lower sideband.)

Analysis of data collected throughout flight showed that the amplitude of the HWPSS was sufficiently large to introduce a nonlinear detector response. (A similar effect was observed by the Polarbear team; Takakura et al. 2017.) EP4 discusses this nonlinear response and a technique to mitigate its effects.

4. Readout

The TES bolometers were voltage biased (Lee et al. 1998). Incident optical power fluctuations modulated the current across the bolometer and across a series inductor and capacitor. A SQUID trans-impedance preamplifier converted the modulated current to a voltage signal that was subsequently further amplified, digitized, and filtered (Yoon et al. 2001).

We used FDM to couple several detectors to a bias and a readout line (Yoon et al. 2001). When the EBEX program began, power dissipation of state-of-the-art analog FDM readout boards consumed approximately 5 W per readout channel, giving a total consumption of nearly 10 kW, a prohibitive level for a balloon-borne payload. We have therefore embarked on implementing a new digital frequency - domain multiplexer (DfMUX) scheme that had approximately 1/10 the power consumption (Dobbs et al. 2008). EBEX was the first experiment to implement this scheme, multiplexing eight detectors with two wires in its 2009 engineering flight, and the first to multiplex 16 detectors in its EBEX2013 flight.

The EBEX readout system required investment of effort along three dimensions: development and testing of the new DfMUX electronic boards, the development of automated onboard software to bias and read the TES bolometers and the SQUID preamplifiers, and the development and implementation of a cooling system that dissipated the 593 W consumed by the DfMUX boards. We discuss only the first element in this paper. The software and cooling system are discussed in EP3. Aubin et al. (2010), Aubin (2012), MacDermid et al. (2014), and MacDermid (2014) give more details about the EBEX readout system.

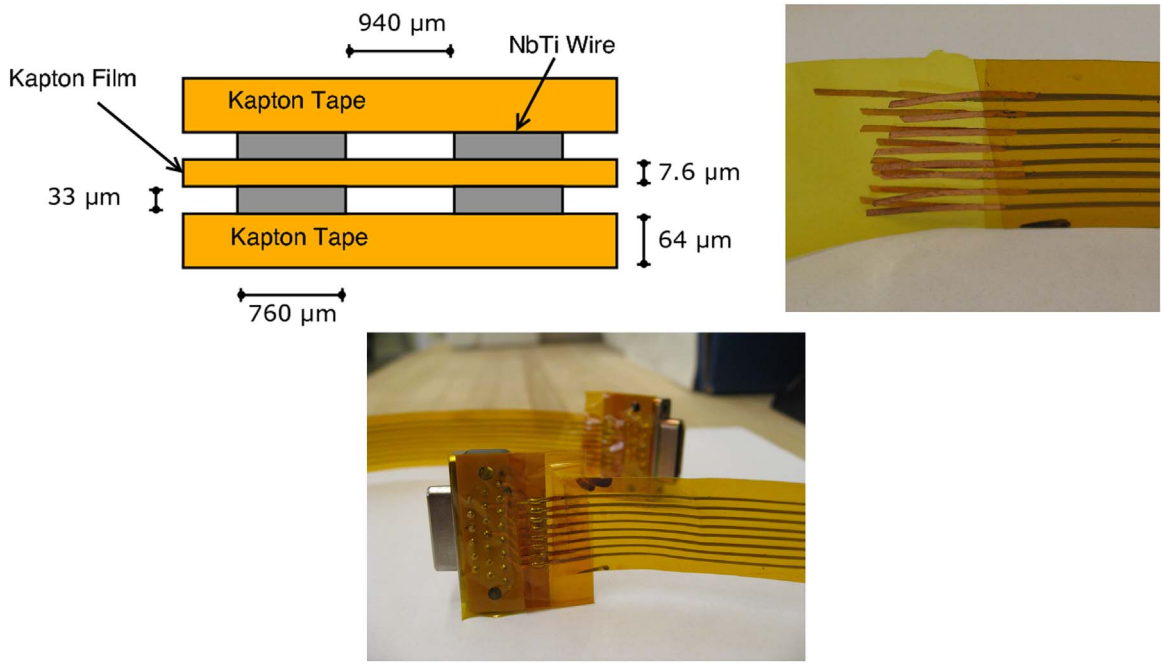

Figure 4. Top left: diagram of the cross section of the microstrip geometry. Two of the eight pairs of wires are shown. Top right: image of copper-clad niobium-titanium wire ends. Bottom: image of the microstrip soldered to micro-D connectors.

4.1. Superconducting Broad-side Coupled Microstrips

During operation, the EBEX TESs had a resistance of approximately 1 Ω. Stray impedance in series with this resistance reduces the detector's voltage bias and causes cross talk. Therefore, we kept the bias and readout wires between the SQUIDs and the LC boards superconducting. Some sections of the wiring were commercially made, but for the longest sections we designed and constructed superconducting broad-side coupled microstrips (Polsgrove 2009; Dobbs et al. 2012).

The microstrips consisted of interleaved layers of kapton and niobium-titanium wires. We selected niobium-titanium because it has a critical temperature of 9.2 K and low thermal conductance in the superconducting state. We chose a parallel-plate waveguide geometry to minimize stray inductance; see Figure 4. We fabricated the flat niobium-titanium wire from 191 μm diameter niobium-titanium wire, which was copper-clad[19] to a total diameter of 305 μm and rolled flat[20] to a thickness of about 33 μm. We dissolved the copper-cladding from the entire length of the flattened wire except for the ends using a nitric acid wash. The copper-cladding remaining at the ends was used to facilitate soldering the wires. The final cross-sectional dimensions of the wires are 760 by 33 μm. To electrically isolate the two wires in each pair, a film of 7.6 μm thick Kapton HN was used as a spacing layer. Adjacent pairs were spaced apart by 940 μm and were secured in their position by a layer of 64 μm thick Kapton HN tape with silicone adhesive. Each microstrip had eight pairs of wires. We measured inductances of 24.5 and 33.3 nH for the 70 and 95 cm EBEX microstrips, respectively.

For each microstrip the ends of the wires were soldered to small flexible circuit boards that had a micro-D connector. The micro-D connectors mated the microstrips to the SQUID boards on one end and to the LC boards on the other. The microstrips were coupled to the SQUID and LC boards with four connectors. We calculated an inductance of 9 nH per connector, giving an estimated total stray inductance of 60.5 and 69 nH for the two lengths. In EP1 we describe the "RF tower" assembly through which the microstrips passed between these two sets of boards. The RF tower gave heat sinking for the microstrips and was part of the RF protection of the receiver.

4.2. Digital Frequency Domain Multiplexing

The EBEX detectors were read out with the DfMUX readout system described in Dobbs et al. (2008). A schematic diagram is shown in Figure 5. For the EBEX2013 flight we implemented a multiplexing factor of 16 (Aubin 2012), the highest used at the time with this readout approach. Ceramic capacitors C_i in series with 24 μH inductors L and the detectors, which had resistance R_i, defined resonant frequencies f_i between 200 and 1200 kHz. The detectors were voltage biased with a 30 mΩ resistor $R_{\rm bias}$, and their output current was nulled to reduce dynamic range requirements. The SQUIDs (Huber et al. 2001) were operated in a shunt feedback with a low-noise transistor op-amp and a feedback resistor $R_{\rm FB}$ of 5 kΩ located on a custom SQUID controller circuit board (Lanting 2006). The wires between the SQUIDs and the room-temperature SQUID controller boards were constrained to be shorter than 33 cm (Dobbs et al. 2008). For longer wire lengths, the phase of the signal shifted by more than 45°, giving positive instead of negative feedback. For EBEX the length of these wires[21] was 19.5 cm. The amplified output bolometer currents were digitized at 25 MHz, demodulated, filtered, and decimated to 190.73 Hz by a field-programmable gate array (FPGA)[22] on each DfMUX board. The data were packetized by a Microblaze virtual processor that was part of the FPGA and

[19] Supercon, Inc.
[20] H. Cross Company.
[21] Tekdata Interconnections Limited.
[22] Xilinx Virtex-4 FPGA.

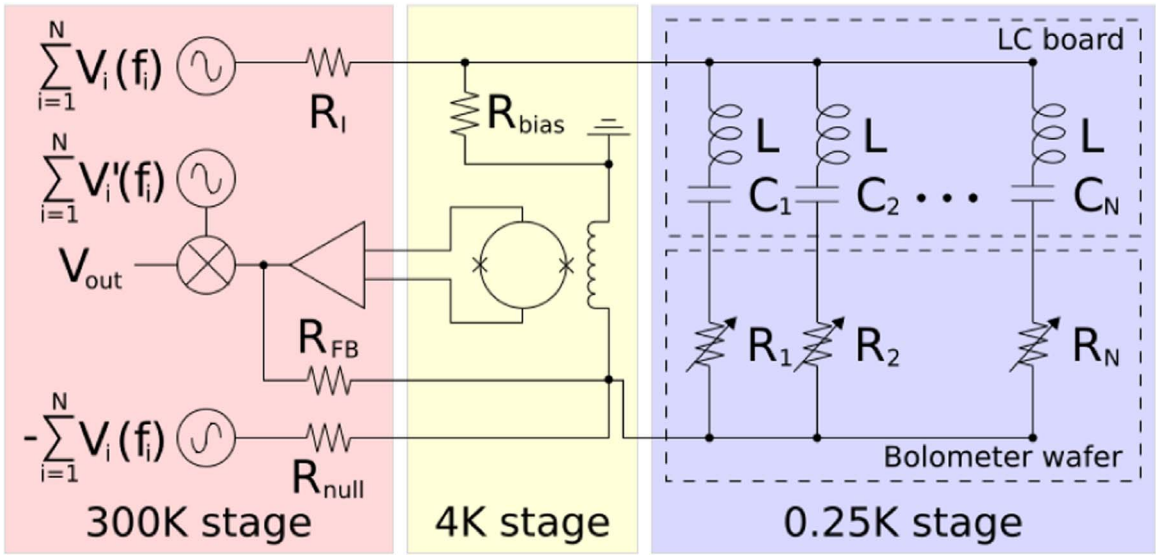

Figure 5. Schematic of the frequency domain readout system (see also Aubin 2012; Dobbs et al. 2008). Colors encode different temperature stages. For the engineering flight N was 8; for the EBEX2013 flight N was 16.

were streamed to the flight control computer over Ethernet for storage, as described in EP3.

We operated 28 DfMUX readout boards and 112 SQUIDs during the EBEX2013 flight. Each board provided biases to and read out four SQUIDs and therefore 64 detectors. The boards were separated into four bolometer readout crates (BRC) each containing either six or eight boards. In addition to the readout boards, each BRC had a VME backplane, a clock distribution board, and an Ethernet communication ring switch. One of the BRCs also held boards that were used to cycle the sub-kelvin refrigerators and read out receiver temperatures. The clock distribution board distributed the 25 MHz clock signal, as well as the commands to turn on/off the boards, and the commands that triggered the reprogramming of the boards' firmware. Each BRC shell acted as a Faraday cage, shielding the readout electronics from RF signals. Two other electronic crates each populated with DC/DCs[23] converted unregulated 28 V to regulated 6 and 10 V (Sagiv 2011; Sagiv et al. 2012). Each crate supplied 296 W to two BRCs; this is 21 W per DfMUX board or 0.33 W per readout channel. Factoring in the 82% efficiency of the DC/DC, the total power consumption of the readout system was 723 W.

The DfMUX onboard "algorithm manager" software listened for JavaScript Object Notation (JSON) formatted requests over TCP/IP issued by the flight control computer via Ethernet communication and executed the requested Python-coded task. The virtual processor of each DfMUX board was programmed to perform tasks in parallel on up to two SQUIDs or the 32 detectors wired to them. These tasks were stored on the DfMUX board flash memory and included tuning the SQUIDs, configuring the voltage biases for the detectors, and ensuring that the SQUIDs were operated within their dynamic range (see more details in MacDermid et al. 2009). With this architecture, we parallelized the array tuning process, saving observing time and reducing the load on the flight control computer. Since each DfMUX board operated four SQUIDs and could perform up to two tasks in parallel, tuning time of the detector array was equivalent to the time to tune two SQUIDs and their associated 32 detectors and was independent of the total number of detectors populating the focal plane. Once the task was completed, the result was sent back to the flight control computer through Ethernet for storage. The interaction between the DfMUX boards and the flight control computer is further described in EP3.

[23] Interpoint Series from Crane Aerospace and Electronics.

4.3. Readout System Noise and Stability

4.3.1. Noise

The term "readout noise" refers to noise contributions from the SQUID preamplifier and the electronic components of the readout system. It excludes the contributions from the detectors that are described in Section 5.5. The performance of "dark SQUIDs" and resistor channels inform the readout noise level independent of detector noise contributions. Unless otherwise noted, we refer to data that were collected during flight. The data were converted from raw digital units (counts) to current through the SQUID by applying the measured transfer function of the readout system dI_b^A/dI_b^c (Aubin 2012),

$$X\ [\mathrm{A}/\sqrt{\mathrm{Hz}}] = X\ [\mathrm{counts}/\sqrt{\mathrm{Hz}}] \cdot dI_b^A/dI_b^c [\mathrm{A}/\mathrm{count}]. \quad (1)$$

The process to generate noise predictions, which are compared to measurements, is described in Aubin et al. (2010) and Aubin (2012). We also include a "current-sharing" noise term that is not described in these publications. This noise term arises because current driven through the SQUID feedback wire is shared between the SQUID input coil and the bolometer. Noise sources originating downstream of the SQUID but inside the feedback loop will result in a feedback current that is enhanced by this sharing. The negative feedback will increase the current, enhancing the noise from these sources (Silva-Feaver et al. 2018). Current sharing depends on the relative size of the SQUID input reactance and the bolometer impedance. To calculate the effect for noise expectations, we use a measurement of the SQUID input inductance for the same SQUID model implemented in a different instrument, ~350 nH, and include it in our noise expectations (Silva-Feaver et al. 2018).

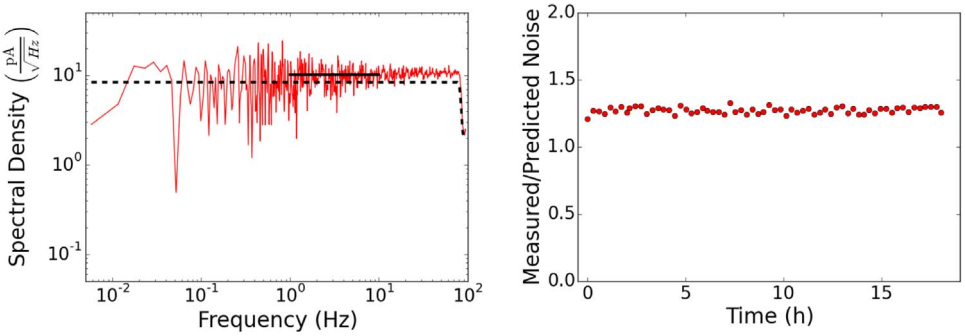

Figure 6. Left: current spectral density of a dark SQUID channel demodulated at 495 kHz. The average level between 1 and 10 Hz (solid red) is 10 $pA/\sqrt{Hz}$. The predicted level (dashed line) is 8.4 $pA/\sqrt{Hz}$. Right: ratio of measured to predicted noise as a function of time for the same channel.

A dark SQUID is a SQUID whose input coil was not connected to detectors or to the sub-kelvin LC boards. Generally, the input wires for a dark SQUID are left open (unterminated) at the 4 K stage; see Figure 5. We demodulated each of the two dark SQUIDs at 16 frequencies within the 200–1200 kHz range typically used to bias detectors. We similarly demodulated two other SQUIDs that became inadvertently dark when they developed an electrical open wire once cooled to 4 K. The current spectral density through the SQUID input coil of a typical dark SQUID for 172 s of data is shown in Figure 6. We select 172 s of data to compute spectral densities in this paper since we high-pass-filter signals above 33 mHz for data analysis. Median predicted noise contributions for the 64 channels are given in Table 1. The ratio of average measured to predicted noise between 1 and 10 Hz for the SQUID channel in Figure 6 is 1.2, which we consider to be broadly consistent with expectations from Table 1, given uncertainties in the transfer functions, component values, and SQUID noise. We use a relatively broad bandwidth to average the noise because we find no evidence for the HWPSS signal with the dark SQUIDs. This noise level is reasonably stable over the entire flight. We show data spanning 18 hr in Figure 6.

To quantify the readout noise over the entire flight and for all dark SQUIDs, we calculated power spectral densities for 172 s sections of data every 20 minutes throughout flight. We found the median measured-to-predicted ratios throughout flight for a given dark SQUID channel. We histogrammed all the channel medians and extracted a single median value representing the performance of the 64 dark SQUID channels; see Figure 7. The 48 well-behaved channels had a median value of 1.2 when the noise is averaged between 1 and 10 Hz. One dark SQUID showed ratios larger than 4 for all of its channels and is considered an aberration. This high-noise SQUID was connected to detector modules but exhibited an open connection in one of its two input wires. We speculate that the other wire acts as a high-impedance antenna, coupling unwanted electromagnetic interference (EMI) into the SQUID input, resulting in high noise.

We also found a consistent median ratio of 1.2 when using measurements on the launch pad, just before flight. Similar measurements performed in two different test cryostats with different SQUIDs gave nominal noise levels, suggesting that the 20% higher median ratio could have a contribution from environmental pickup, differences in the SQUIDs, or signals coupled from elsewhere in the instrument. A ∼5% variation is measured between the lowest- and highest-frequency channels, which is likely caused by the omission of stray inductance in the noise prediction.

Table 1
Components of the Predicted Post-demodulation Noise for Dark SQUIDs

Noise Source	Value $pA/\sqrt{Hz}$
SQUID	$\sqrt{2} \cdot 3.5$
Demodulation chain	$\sqrt{2} \cdot 3.8$
Nuller chain	$\sqrt{2} \cdot 2.4$
Total	$\sqrt{2} \cdot 5.7$

Note. SQUID noise of 3.5 $pA/\sqrt{Hz}$ is typical for our devices (NIST 2010, private communication). The explicit factors of $\sqrt{2}$ are due to uncorrelated power on both sides of the demodulation frequency. The nuller chain noise is dominated by resistor Johnson noise when not providing nulling currents.

Resistor channels had the entire readout chain coupled to 1 Ω resistors that were mounted on the LC boards. The noise for the resistor channels consists of both Johnson and readout noise terms. The total noise with these channels represents a cross-check on measurements of the detectors' noise when they were biased above their superconducting transition, as discussed in Section 5.5. The analysis of the data parallels that of the dark SQUIDs. Figure 7 shows the distribution of the median measured-to-predicted noise ratio for 16 well-behaved resistor channels throughout flight; five additional resistor channels had a noise ratio more than 3.5 times the median and were excluded from the analysis. The resistor channels have a median measured-to-predicted noise ratio of 1.7. The resistors are mounted on the 0.25 K stage. We hypothesize that wires of 70–95 cm long from the SQUIDs act as antennas allowing electromagnetic pickup to couple to the SQUID input, producing excess noise. Coupling such as this can produce narrowband features in noise spectra if the EMI lies in the carrier bandwidth, resulting in detector-by-detector variations, or broadband white noise if the EMI is away from the carrier bandwidth but coupled to the SQUID. Another potential increase in noise is another detector, or detectors, sharing the same SQUID and thus the bias lines for same comb of frequencies. For example, a "latched" detector—a detector operating below the superconducting temperature—increases the noise level for all other readout channels on the same comb.

After the EBEX North American engineering flight, noise was measured in the laboratory with detectors above the superconducting transition. As we discuss in more detail in Section 5.5.1, in terms of readout chain noise expectations, this

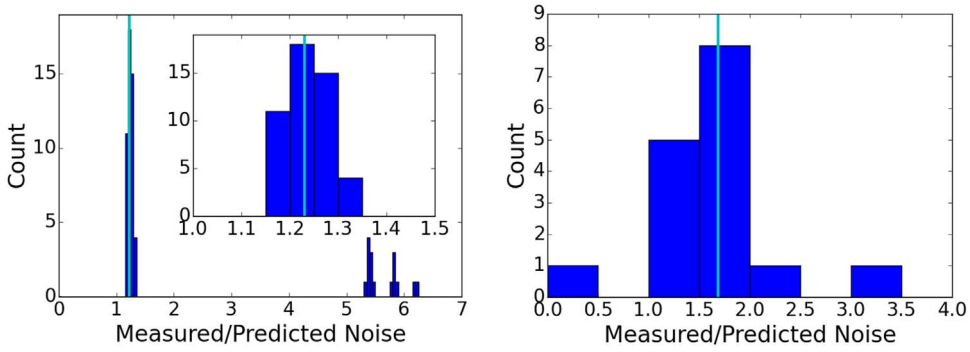

Figure 7. Left: distribution of measured-to-predicted noise ratio for the 64 dark SQUID channels. The median for the 48 well-behaved channels (vertical cyan) is 1.2. Right: distribution of measured-to-predicted noise ratio for the 16 resistor channels. The median (vertical cyan) is 1.7.

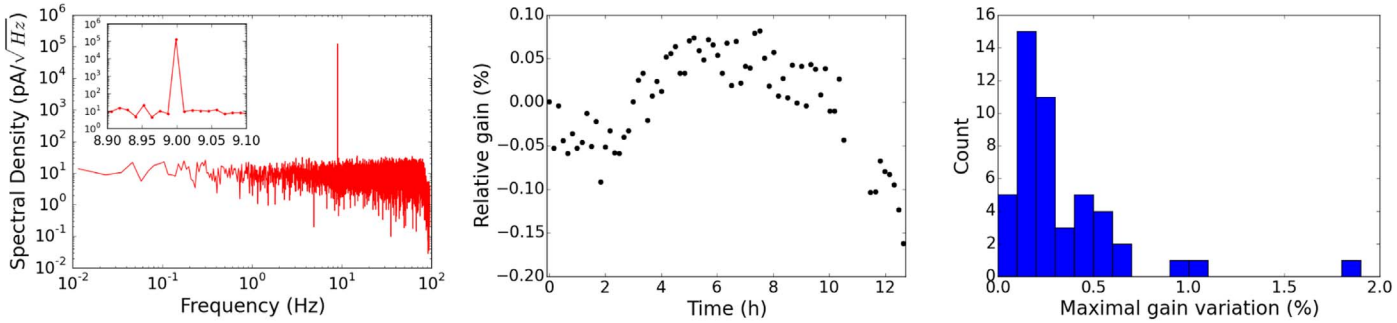

Figure 8. Left: current spectral density for one gain-monitor channel. The sharp line at 9 Hz is the demodulated nuller current provided to the SQUID coil at 110 kHz and demodulated at 110 kHz + 9 Hz. Middle: time variation of the readout gain for one channel during 12.7 hr. The maximal peak-to-peak gain variation is 0.25%, which is negligible compared to the overall calibration uncertainty. Right: distribution of the maximal gain variation measured at two frequencies for 12 SQUIDs for multiple segments of the EBEX2013 flight.

configuration is similar to the resistor channel setup for the science flight. The ratio of measured to predicted noise was 1.0 ± 0.1 (Aubin et al. 2010), which suggests that the excess resistor noise measured in the science flight is an environmental effect, rather than inherent to the readout chain. We revisit and discuss this again in Section 5.5.1.

We find no evidence for correlated noise between the data of any of the dark channels. Using 18 contiguous time sections, 86 s each, we calculate the coherency (Priestly 1981) of all pairs of channels.[24] We compare the average coherency between all pairs to the expectation for white noise, which with our data is 0.029. We find a coherency of 0.0253 with a dispersion of 0.0002 for dark SQUIDs and 0.035 with a dispersion of 0.009 for resistor channels.

4.3.2. Gain Variations

We monitored gain fluctuations of the readout system by using 24 unused readout channels distributed over 12 SQUIDs, which also read out live detector channels, a pair per SQUID. For these channels, no biases were supplied through the carrier wire since they are operated far from any LC resonance in the cold multiplexer; see Figure 5. Instead, we injected two small constant sinusoidal currents, one at 110 kHz and the other at 1260 kHz, into the input coil of the SQUID using the nuller wire. These frequencies were 60 kHz above and below our standard lowest and highest bias frequencies. The amplitudes were either 30 or 100 nA. The signals were demodulated at a frequency 9 Hz higher than the nulling current, resulting in a 9 Hz demodulated sinusoidal current; see Figure 8. These data were then processed like all other bolometer data.

Since the injected current was constant, amplitude modulation of the demodulated signal is an indication of readout gain variation. The variation of gain for one channel over 12.7 hr of flight is shown in Figure 8. This particular channel experiences a gain change of 0.25%. The data points are from 85.9 s sections of data separated by 10 minutes. A histogram for all gain monitoring channels gives a stability that is mostly better than 1%. Over the same period of time temperature sensors on the readout boards indicate board temperature changes of up to 20°C. We measure in the laboratory that a similar temperature change of one readout board causes its gain to change by up to 0.3%. We conclude that gain variations of the readout system are negligible compared to the overall calibration uncertainty, which is $\gtrsim$10%.

5. Detectors

EBEX uses spider-web TES bolometers. We optimized the parameters of the bolometers for cosmological observation from a balloon platform. In this section we describe the design characteristics of the EBEX bolometers and report on measurements of their normal resistance, thermal conductance, critical temperature, time constant, and optical efficiency. We use these measurements in combination with the measured absorbed power by the detectors to predict the noise performance of the detectors. We finally compare these predictions to data to assess their in-flight performance.

[24] The coherency of two time series is the ratio between their cross-spectra and the product of their auto-spectra.

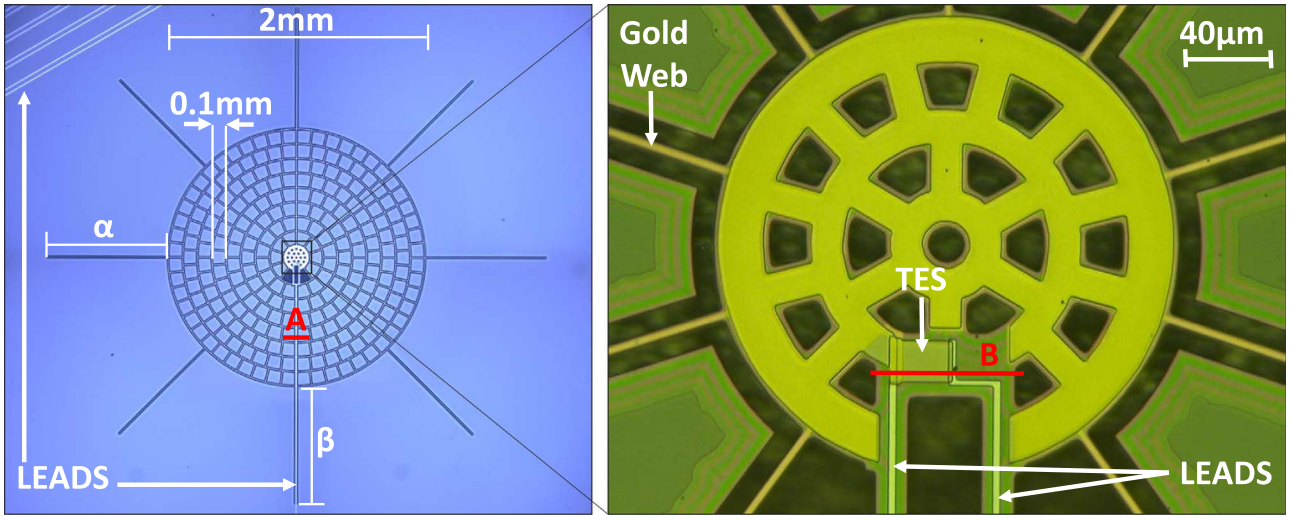

Figure 9. Left: photograph of an EBEX bolometer. Right: enlargement of its central region. The leg with length β was 17 μm wide to accommodate the niobium leads. The other seven legs (with length α) were 6 μm wide. Table 2 gives the dimensions of the parameters α and β. Red lines labeled "A" and "B" indicate cross sections that are shown in Figure 10.

Table 2
Designed and Measured Detector Parameters for Each of the Frequency Bands

Parameter	150 GHz		250 GHz		410 GHz	
	Design	Measured	Design	Measured	Design	Measured
R_n (Ω)	1.5	1.9	1.5	1.5	1.5	1.4
T_c (K)[a]	0.44	0.45	0.44	0.48	0.44	0.47
$\overline{G}$ (pW/K)	19	39	45	54	63	63
τ_0 (ms)	17	88[b]	13	46[b]	10	57[b]
C (pJ/K)[c]	0.5	3.8[b]	0.9	3.3[b]	1.0	8.4[b]
Wafer thickness (μm)	150		90		56	
α (mm)	1.05		1.0		0.5	
β (mm)	1.45		1.0		0.5	

Notes. The values in the "measured" columns are median values for all detectors on wafers used for flight. Description of the measurements, histograms, and further discussion of the measured values are given in Section 5.2. For the parameters α and β shown in Figure 9 we give the design values. The lithography was generally accurate to within 0.5 μm.
[a] Design values calculated early in the program using thermal conductivity power index $n = 3$ and a bath temperature of 260 mK.
[b] Median of measurements on a single wafer at each frequency; see Section 5.2.4.
[c] Calculated from time constant and thermal conductance.

5.1. Detector Design

The detectors had spider-web absorber architecture similar to the TESs used for the APEX-SZ and SPT-SZ experiments (Lee et al. 1996; Chang et al. 2009; Schwan et al. 2011; Westbrook et al. 2012; Westbrook 2014). The design of a single TES, shown in Figure 9, consisted of a low-stress silicon nitride, gold-metalized web that served as the absorber for millimeter-wave radiation. The web was suspended above the silicon wafer by eight legs, which provided thermal isolation and were used to tune the thermal conductance of the bolometers. A TES made of aluminum-titanium superconducting proximity bilayer in the middle of the web was operated at its transition temperature, typically between 0.4 and 0.5 K. Two niobium leads delivered constant voltage bias and monitored current fluctuations.

Table 2 gives the bolometer design parameters for the three EBEX frequency bands, including the TES electrical resistance in the normal state (R_n), TES transition temperature (T_c), average thermal conductance ($\overline{G}$), bolometer geometry parameters α and β described in Figure 9, the expected heat capacity (C) of the bolometers, and the intrinsic optical time constant (τ_0). The choice of some of the design parameters, most notably the thermal conductance, reflects the unique demands of a balloon flight; the in-flight optical loading is not a priori known, and once the instrument is conducting observations, there is no opportunity for further detector optimization. Therefore, the thermal conductance must have sufficient margin, that is, must be large enough, to ensure that the detectors can operate over a relatively broad range of optical loadings. A consequence is that with nominal optical load a larger detector voltage bias is required, which reduces the responsivity and amplifies readout NEP.

5.1.1. TES, Absorber, and Backshort

The TESs were constructed from a 110 nm titanium layer deposited on top of a 40 nm aluminum layer in a single vacuum step. We chose a transition temperature of 0.44 K to minimize phonon noise given the expected 0.25 K focal plane temperature (Suzuki 2013). The normal resistance for all bands

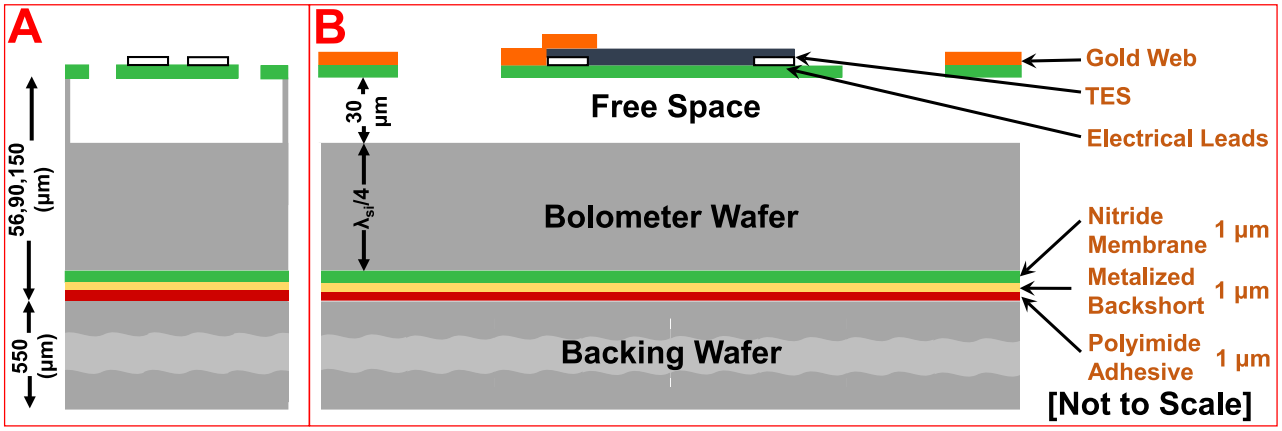

Figure 10. Cross sections through the lines "A" and "B" from Figure 9 showing the layers of the EBEX detectors through the thermal isolation leg carrying the electrical leads (A) and the central portion of the bolometer that carries the TES (B). The thickness of bolometer wafer depended on frequency band; see text. The bolometer wafer was bonded to a thicker backing wafer to provide mechanical stability during fabrication. A metallic layer deposited on the back side of the detector wafer provided a backshort for increased absorption. An aluminum-titanium bilayer forms the TES of the bolometer at the center of the pixel.

was 1.5 Ω to ensure that the detector operated in the stable regime (Dobbs et al. 2012).

A metalized spider-web structure appears as a continuous sheet of metal with resistivity $\rho_{\rm web}$ to electromagnetic radiation of wavelength λ incident upon it as long as the grid spacing g satisfies $g \ll \lambda$ (Bock et al. 1995). In addition, the return loss remains below −10 dB when $\rho_{\rm web}$ is between 150 and 700 Ω/sq (Glenn et al. 2002). The EBEX web grid spacing was 100 μm, 7 times smaller than the shortest wavelength admitted, and we used a 200 Å thick layer of gold to achieve $\rho_{\rm web} = 350$ Ω/sq.

The absorption efficiency of the detector depends on the distance of the backshort from the absorber. Within a single uniform silicon medium the optimal distance is $\lambda_c/4$, where λ_c is the wavelength in solid silicon behind the web absorber; $\lambda_c = \lambda_0/n_{\rm Si}$, where λ_0 is the wavelength in empty space and $n_{\rm Si} = 3.4$ is the index of refraction of silicon (Lamb 1996; Rownd et al. 2003). To achieve these backshort thicknesses, we etched the detector wafers to thicknesses of 150, 90, and 56 μm for the 150, 250, and 410 GHz bands, respectively. However, these wafer thicknesses were too thin to survive standard microfabrication techniques, and we thus bonded the bolometer wafer to a thicker backing wafer to provide additional mechanical stability (Westbrook et al. 2012; Westbrook 2014); see Figure 10.

When we include in the absorption simulation the 30 μm cavity behind the web absorber, which makes the backshort a combination of two media, we find that the expected absorption efficiency is 35% at 410 GHz and 75% for the other two bands.

5.1.2. Thermal Conductance

Table 2 gives our specifications for the average thermal conductance for each of the frequency bands. We arrived at these specifications by conservatively requiring that the bolometer handle total absorbed powers of up to 4, 9, and 12 pW for each of the 150, 250, and 410 GHz bands, respectively, before the TES exits the superconducting transition. We set these requirements early in the development of the instrument by calculating the expected optical loads from both sky and instrument sources and by applying a safety factor to account for unexpected loads. We find that our conservative specifications are met when comparing to the measurement of the in-flight total optical load described in Section 5.3.

Of the two contributions to the thermal conductance of the bolometer, (i) the silicon nitride legs that connected the web to the wafer and (ii) the two niobium electrical leads, the thermal conductance of the niobium leads was negligible (Kes et al. 1974; Westbrook 2014). Therefore, we achieved different thermal conductances for each frequency band through changes in the geometry of the silicon nitride legs. The geometry of the legs and the calculated average thermal conductances are given in Figure 9 and in Table 2.

5.1.3. Intrinsic Time Constant

The intrinsic optical time constant of the bolometer τ_0 is set by the ratio of the heat capacity C at the operating temperature to the differential thermal conductance $G = dP/dT$: $\tau_0 = C/G$. The predicted heat capacity of the bolometer was dominated by the contributions of the TES and the gold absorber layer, which gave 80% and 20% of the total, respectively. The calculated contributions of the silicon nitride web and niobium leads were calculated to be negligible (Van Sciver 2012; Westbrook 2014). Since the TES and gold layer were identical among the frequency bands, changes in the time constant with frequency band were a result of differences in thermal conductance. Table 2 gives the design values of τ_0 for each of the frequency bands. The table quotes the average thermal conductance $\overline{G}$, which is related to the differential value through

$$G = (n+1)\left(\frac{1-\left(\frac{T_0}{T_c}\right)}{1-\left(\frac{T_0}{T_c}\right)^{n+1}}\right)\overline{G}, \quad (2)$$

where T_0 is the bolometer bath temperature, and following conventions, we assumed power-law dependence for the differential thermal conductance $G = gT_c^n$. We used $n = 2$ since thermal conductivity measurements of engineering flight wafers gave values of 2.2 ± 0.3, 1.9 ± 0.2, and 2.1 ± 0.2 for the 150, 250, and 410 GHz bands, respectively (Hubmayr 2009; Aubin et al. 2010).

Table 3
Detector Yield Tally by Frequency Band

	Count of	Frequency (GHz) 150	250	410	Total
1	Detectors on wafers	1120	560	280	1960
2	Maximum detectors to read out	992	496	254	1742
3	Detectors that passed warm electrical & visual inspections	908	455	232	1595
4	Channels wired to detectors that passed warm electrical and visual inspections	861	447	213	1521
5	Detectors that passed the 0.8 K network analysis test	805	430	187	1422
6	Detectors after SQUID failures removed	773	414	155	1342
7	Detectors after noise polluters removed	676	371	133	1180
8	Detectors with successful flight I-V curves	504	342	109	955

5.2. Detector Characterization

We characterized the properties of all 14 detector wafers that were included in the EBEX2013 flight. Characterization included testing for electrical continuity of each detector before a wafer was wire-bonded with an LC board and a standard set of measurements at cryogenic temperatures in dark conditions. In dark conditions, the wafer was mounted inside a sealed box cooled to 0.32 K and thus was subjected to an optical power load of ∼9 fW, which is two orders of magnitude smaller than expected in-flight conditions.

There were 140 bolometers fabricated on a single EBEX wafer, of which we could read out 124 with the edge and 127 with the central LC boards. This gave a total of 1960 bolometers, from which 1742 could be read out, as listed in the first two lines of Table 3. We now enumerate further reductions in detector yield. At room temperature, each bolometer was inspected visually under a microscope and also probed across its bond pads for electrical continuity (line 3). To monitor noise, some electronic channels read out resistors located on the LC boards (two per wafer), four combs were attached to dark SQUIDs that did not have bolometers, and one SQUID had an electronic malfunction (line 4). Some bolometers that had electrical continuity at room temperature did not have continuity during the cold (0.8 K) network analysis (line 5). Of the 112 SQUIDs, 5 failed to tune (line 6). Those bolometers whose operation drastically worsened the noise performance of their entire comb were disconnected (line 7). The number of bolometers that had successful I-V curves during first tuning at float is given in line 8.

5.2.1. Resonant Frequencies

We determined the resonant frequencies for each comb of frequencies by maintaining the detectors at 0.8 K, that is, above their transition temperature, and sweeping the bias frequencies between 0.1 and 1.3 MHz. The RLC circuit resonated at its characteristic frequency such that the entire sweep gave a response as shown in Figure 11. A fit of the peak of the resonance with a model of the circuit that accounts for current leakage to all resonators gave the resonant frequencies and the normal resistances of the TESs in the comb (Aubin 2012). Missing peaks in this measurement corresponded to opens in electrical lines.

Figure 12 gives histograms of the measured normal resistance R_n values for each frequency band. The 150 and 410 GHz bimodal distributions were due to detector parameters being closely grouped within a single fabrication run, but varying between fabrication runs. The measured value of R_n for the 250 GHz band closely matched the design (see Table 2). For the other two frequency bands, one mode of the distribution closely matched while the other mode was higher (lower) than design for the 150 (410) GHz band. The 150 GHz detectors with a measured R_n of 1.9 Ω, instead of the nominal 1.5 Ω, were calculated to have increased electrical cross talk from a value of 0.5%–0.8% and decreased loop gain by 30%. The 410 GHz detectors with a measured R_n of 1.4 Ω were calculated to have increased Johnson noise by 4% relative to the nominal expected value of 4.0 $\mathrm{pA}/\sqrt{\mathrm{Hz}}$.

5.2.2. Transition Temperature

For the measurement of the critical temperature T_c we biased the detectors with 5 nV such that the Joule heating of 1.5 fW was small and the bath temperature was a good proxy for the bolometer's temperature. For the same reason, the measurement was done in dark conditions. We slowly changed the detectors' temperature while monitoring the current through the TES. At the critical temperature the current showed a steep transition. Figure 13 shows histograms summarizing the measured critical temperatures. There was a ∼20% wafer-to-wafer spread in the measured T_c with the medians for the three bands within 11% of the target value of 0.44 K. The 150 GHz detectors have the widest spread of measured T_c. The effect of this spread is twofold: (1) it increases Johnson (phonon) noise when T_c is above (below) the design value, and (2) it increases (decreases) the detector saturation power when the T_c is above (below) the design value. At the high (low) edge of the distribution with $T_c = 0.59$ K (0.34 K), there was a 16% (14%) increase (decrease) in the calculated Johnson noise relative to the nominal expected value of 4.0 $\mathrm{pA}/\sqrt{\mathrm{Hz}}$ and an 80% (68%) increase (decrease) in the calculated phonon noise relative to the nominal expected value of 13 $\mathrm{aW}/\sqrt{\mathrm{Hz}}$. On the low edge of the distribution, the critical temperature causes the 150 GHz detectors to saturate, leaves the responsivity unchanged for the 250 GHz bolometers, and increases the responsivity by 66% for the 410 GHz bolometers. The responsivity is decreased by 110%, 56%, and 60% for the 150, 250, and 410 GHz bolometers, respectively, on the high edge of the distribution, increasing the readout and Johnson noise relative to phonon and photon noise.

5.2.3. Average Thermal Conductance

We determine the average thermal conductance of the bolometers using the relation

$$\overline{G}(T_0) = P_{\mathrm{sat}}(T_0)/(T_c - T_0). \quad (3)$$

The "saturation power" P_{sat} is the power necessary to operate the TES in the regime of strong electrothermal feedback in which the total power absorbed is constant. This power

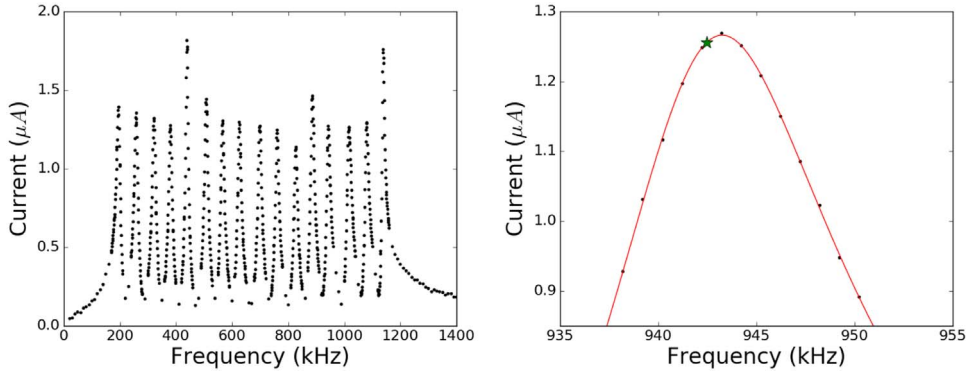

Figure 11. Left: current response of a multiplexed detector circuit as a function of bias frequency. Right: zoom-in on one peak (black dots) with the fitted response (red line) and the optimal bias frequency (green star) minimizing cross talk (Aubin 2012).

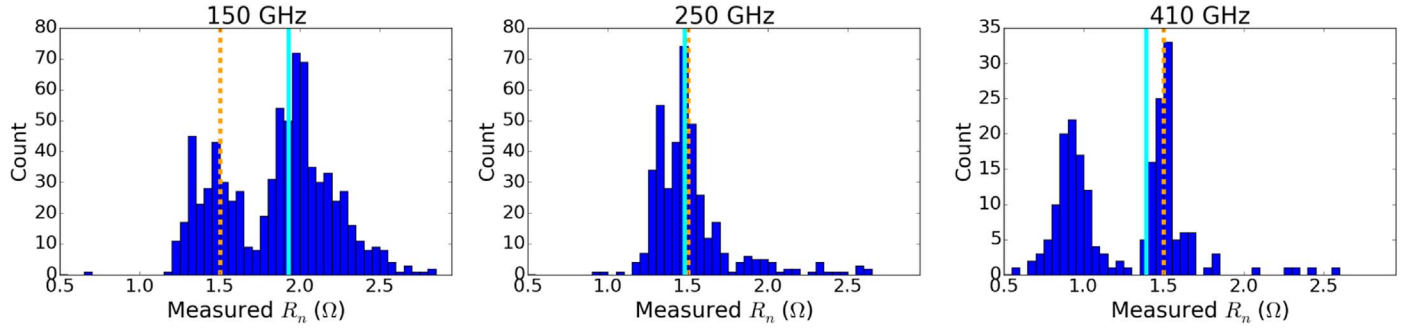

Figure 12. Histogram of measured normal resistances R_n for each of the frequency bands, including the median (vertical cyan) and design (vertical gold dashed) values.

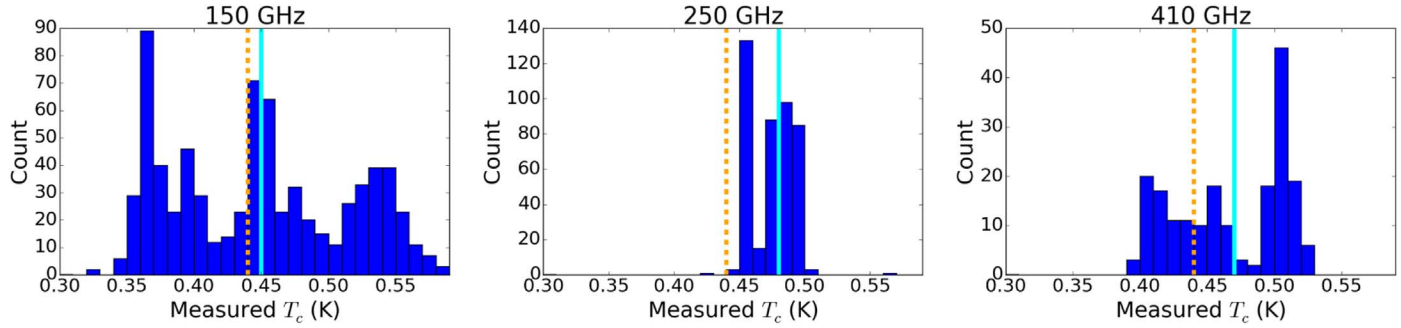

Figure 13. Histogram of measured critical temperature values for the detectors in each frequency band including the median (vertical cyan) and design (vertical gold dashed) values.

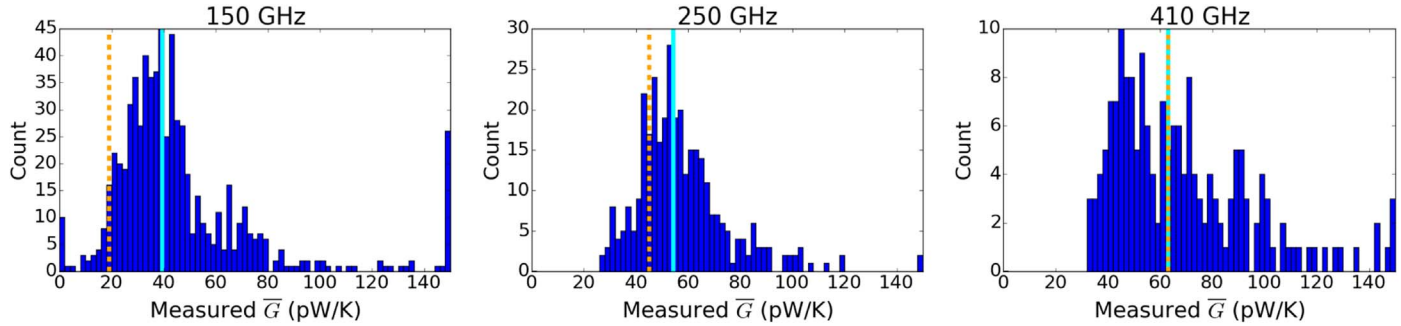

Figure 14. Histograms of the measured average thermal conductance values for the three frequency bands, including the median (vertical cyan line) and design (vertical gold dashed line) values. We piled measurements of $\overline{G}$ exceeding 150 pW/K into the last histogram bin.

depends on the bath temperature

$$P_{\rm sat}(T_0) = P_e(T_0) + P_{\rm abs}. \quad (4)$$

Here P_e is the electrical power absorbed in Joule heating and $P_{\rm abs}$ is the radiative power absorbed. In dark conditions we assume that $P_{\rm abs} = 0$, and so $P_{\rm sat}(T_0) = P_{e,d}(T_0)$ is therefore a

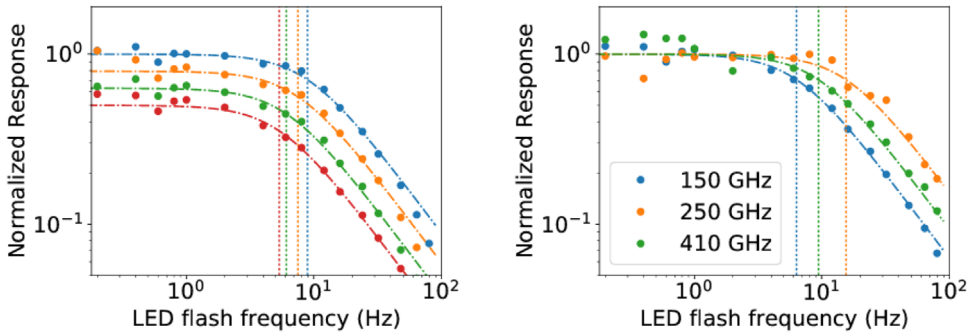

Figure 15. Examples of the measured, normalized temporal response of bolometers as a function of LED flash frequency (circles), the single-pole response fits (dot-dashed lines), and the 3 dB point (vertical dotted lines). Left: response of four 150 GHz bolometers biased at $0.8R_n$. The normalized response is offset vertically for clarity. Right: response of one bolometer per frequency. All three were tuned to $0.8R_n$.

measurable quantity; we added the subscript d to $P_{e,d}$ to highlight that this is the electrical power measured in dark conditions.

Histograms summarizing the measured average thermal conductance values for the three EBEX frequency bands are shown in Figure 14. The values of $\overline{G}$ are given for the EBEX bath temperature $T_0 = 0.25$ K. The measurements were conducted in three different cryostats, each operating at a different bath temperature $T_{0'}$. We corrected the measured values $\overline{G}(T_{0'})$ to $\overline{G}(T_0)$ using the scaling

$$P_{\rm sat}(T_0) = \left(\frac{T^{n+1} - T_0^{n+1}}{T^{n+1} - T_{0'}^{n+1}}\right) P_{\rm sat}(T_{0'}), \tag{5}$$

which assumes that the differential thermal conductance follows a power law $G \propto T^n$; see Section 5.1.3. The design and median of measured values for the average thermal conductances are given in Table 2. There is appreciable spread in the measured values. This spread is a consequence of variance between wafers and is also apparent in the measurements of T_c. Higher thermal conductance increases phonon noise. For example, for a median 250 GHz detector, phonon noise increased by 10% relative to the nominal value of 20 aW/$\sqrt{\rm Hz}$. Higher thermal conductance also increases the required electrical power, decreasing responsivity, which scales as $1/V_{\rm bias}$. With a lower responsivity, noise sources that produce fixed current such as readout noise are referred to higher NEP values. In this manner, higher thermal conductance effectively amplifies readout noise.

5.2.4. Detector Time Constants

The effective time constant of the bolometer is given by

$$\tau_{\rm eff} = \frac{\tau_0}{1 + \mathcal{L}}, \tag{6}$$

where $\mathcal{L}$ is the loop gain of the bolometer (Lee et al. 1998).

During the course of the EBEX project, we measured time constants in various configurations, including a flashing light-emitting diode (LED) as part of "dark" measurements, chopping between two optical loads (Hubmayr 2009; Polsgrove 2009), using the phase and amplitude methods during polarization calibration, as described in EP1 and in Klein (2014), and assessing the shapes of cosmic-ray events during flight. Here we report the results from measurements conducted post-flight on three wafers. In contrast with previous measurements, the post-flight ones were all done in identical conditions, using the same method, and have good detector statistics. Each of the three wafers had detectors fabricated for a different frequency band. For the 150, 250, and 410 GHz band wafers there were 88, 97, and 88 active bolometers, respectively.

We used a dedicated cryostat to operate one wafer at a time in dark conditions and at a bath temperature of 0.32 K. We measured $\tau_{\rm eff}$ at various operating points along the superconducting transition as quantified by fractions of bolometer normal resistance R_n. We used LEDs with a center wavelength of 940 nm and intrinsic time constant of 1 μs to excite the bolometers. The LED was flashed on/off at 13–16 frequencies from 0.1 to 80 Hz for 2 minutes at each frequency. We calculated the power spectral density (PSD) of the time stream, removed the background, fit a Fejer kernel (Weiße et al. 2006) to the peak centered on the flash frequency, and extracted the power under the peak from the fit. We plot the response as a function of flash frequency, fit to a single pole function

$$R(f) = \frac{A}{\sqrt{1 + (f/f_c)^2}}, \tag{7}$$

where A is an arbitrary amplitude at $f = 0$, extract the 3 dB cutoff frequency f_c, and convert it to the bolometer time constant

$$\tau_{\rm eff} = \frac{1}{2\pi f_c}. \tag{8}$$

Figure 15 shows a selection of these measurements that are normalized to unity through division by their normalization values A. For each measurement we extracted the error δf_c from the fit's covariance matrix and propagated it to calculate $\delta\tau_{\rm eff}$. We kept those measurements of $\tau_{\rm eff}$ for which $\delta\tau_{\rm eff}/\tau_{\rm eff} < 0.5$ and $\delta\tau_{\rm eff} < 10$ ms. For each wafer the cuts removed between 20% and 50% of the measurements at each point in the transition.

The measured distributions of $\tau_{\rm eff}$ for the 150 GHz bolometers are shown in Figure 16. For each wafer and transition depth we found the median of the distribution and plotted the medians as a function of transition depth. On all three wafers the width of the distribution was dominated by variations between detectors rather than measurement errors; typical $\delta\tau_{\rm eff}$ values were 1 ms. For all three wafers $\tau_{\rm eff}$ qualitatively followed the expectation of $1/(1 + \mathcal{L})$, since $\mathcal{L}$ increases deeper in the transition; see Figure 16.

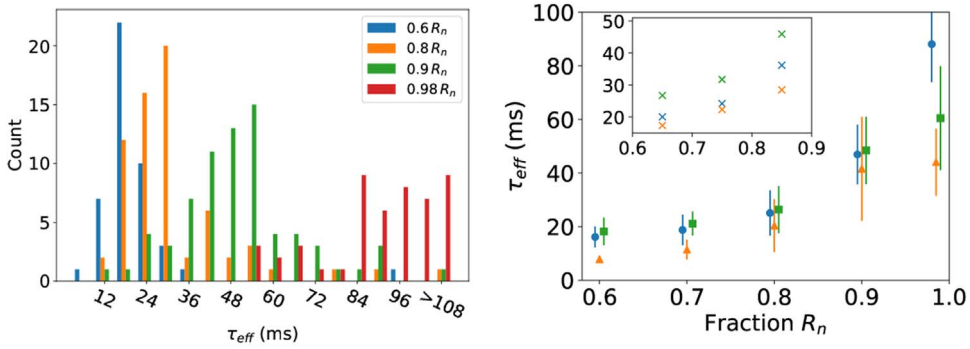

Figure 16. Left: distributions of measured $\tau_{\rm eff}$ for the 150 GHz wafer at four depths in transition. Right: median $\tau_{\rm eff}$ as a function of the fraction of R_n for the different frequency bands—150 GHz (blue circles), 250 GHz (orange triangles), and 410 GHz wafer (green squares). Error bars are the standard deviation of the $\tau_{\rm eff}$ distributions at each transition depth. We extrapolated laboratory measurements to flight conditions to estimate median time constants at the three transition depths used in flight (inset).

We measured τ_0 by assuming $\mathcal{L} \ll 1$ at the highest bias point, $0.98R_n$, so $\tau_{\rm eff} \approx \tau_0$; median τ_0 values are given in Table 2. They are longer than design values by factors of 4–6. We combined the measurements of τ_0 with independent measurement of G to infer bolometer heat capacities. For each bolometer we calculated G according to Equation (2) using measured $\overline{G}$, T_c, n, and a 0.32 K bath temperature. We calculated C for each bolometer and give the design and median of measured values in Table 2. We find that the median heat capacities are larger than design values by factors of 4–8. There are two possible sources for larger-than-expected heat capacities: larger specific heats or larger volumes. We measured the thicknesses of the various layers deposited to make the bolometers and find that the volumes were within 15% of design values.

We provided an approximate value for the time constants in flight by extrapolating the thermal conductance to the in-flight 0.25 K bath temperature and by accounting for changes in $\mathcal{L}$ due to the lower electrical bias of the detectors, which was a consequence of higher in-flight optical load. We did not attempt to correct $\mathcal{L}$ for differences in $\alpha = d(\log R)/d(\log T)$ because the derivatives dr/dT were noisy. The calculated $\tau_{\rm eff}$ for the three bias points used in flight are shown in Figure 16. During the majority of flight, bolometers were tuned to $0.85R_n$.

5.3. Radiative Load

Equation (4) quantifies the balance of power between a bolometer and its thermal bath when the total power absorbed $P_{\rm abs}$ is constant. $P_{\rm sat}$, which depends on the thermal conductance, transition temperature, and bath temperature, has a characteristic value for each detector and was measured for the majority of the detectors in dark conditions. Although these measurements were done at different bath temperatures $T_{0'}$, they were corrected to the operating temperature in flight T_0 using Equation (5). We use Equation (4) to infer the radiative power absorbed in flight

$$P_{{\rm abs},f} = P_{\rm sat}(T_0) - P_{e,f}(T_0) = P_{e,d}(T_0) - P_{e,f}(T_0), \qquad (9)$$

where the subscripts d and f denote dark and in-flight conditions, respectively. Figure 17 shows an example of a 150 GHz detector for which $P_{{\rm abs},f} = 4$ pW. The electrical power dissipated is plotted as a function of the voltage across the bolometer in dark and flight conditions; these are commonly called "load curves." The difference of 4 pW is measured at the lowest power points of the two load curves, the points at which the bolometer had just entered the constant

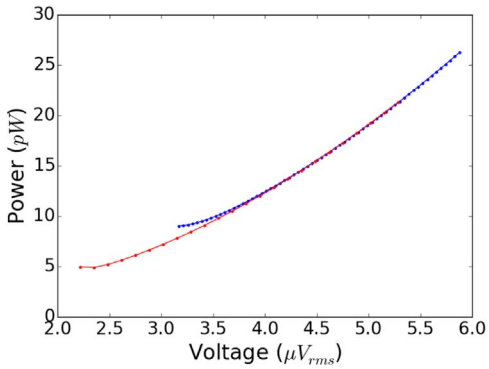

Figure 17. Measurements of load curves of a 250 GHz detector in dark conditions (blue) and during flight (red). The detector is operated with voltage bias such that the total power is constant, which is approximately 9 pW in dark conditions. Only 5 pW of electrical power are necessary in flight because absorbed radiative power makes up the difference.

power operating regime. To ensure stability, we operated the detectors as they just entered this regime, that is, relatively high in the superconducting transition. For the majority of the flight the detectors were operated at 85% of their normal resistance.

Figure 18 shows the distribution of the radiative load measured by all detectors. We used the load curves measured during the first tuning at float altitude. The elevation (zenith) angle of the telescope was 60° (30°). We measure an average load of 3.6, 5.3, and 5.0 pW for the 150, 250, and 410 GHz detectors, respectively.

5.4. Optical Efficiency

The end-to-end instrument efficiency for a given detector, defined as the ratio of radiative power absorbed by the detector $P_{\rm abs}$ to the radiative power incident on the instrument $P_{\rm inc,inst}$, is the product of the telescope's transmission ϵ_t and the bolometer absorption efficiency ϵ_b,

$$\epsilon = \frac{P_{\rm abs}}{P_{\rm inc,inst}} = \epsilon_t \frac{P_{\rm abs}}{P_{\rm inc}} = \epsilon_t \epsilon_b. \qquad (10)$$

Here $P_{\rm inc}$ is the radiative power incident on a bolometer.

The transmission of the telescope is the product of the transmissions of each of the optical elements. These transmission coefficients were measured or calculated from first principles (Aubin 2012; Zilic 2014) and are summarized in Tables 4 and 5 for the flight and ground measurement

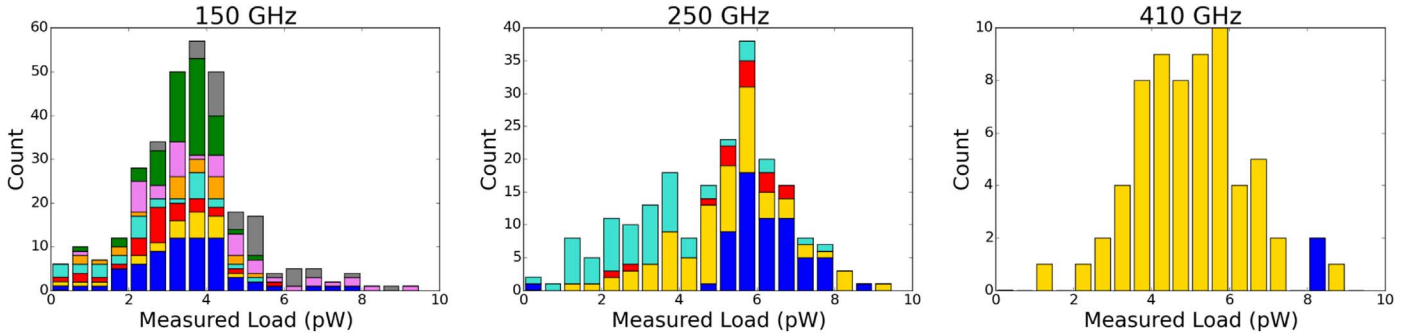

Figure 18. Histograms of the measured radiative load from the first detector tuning at float. The different colors represent different wafers. The medians and standard deviations of the distributions are 3.6 ± 1.5 pW, 5.3 ± 1.8 pW, and 5.0 ± 1.4 pW for the 150, 250, and 410 GHz, respectively.

Table 4
Optical Elements Used during Flight and Their Transmission for Each of the Frequency Bands

Element	150 GHz	250 GHz	410 GHz
Primary mirror	1.00	1.00	1.00
Secondary mirror	1.00	1.00	1.00
Cryostat window	0.97	0.96	0.97
Thermal filter type 4	0.95	0.95	0.95
Thermal filter type 4	0.95	0.95	0.95
Thermal filter type 3	0.98	0.98	0.98
Teflon filter	0.96	0.95	0.93
Thermal filter type 3	0.98	0.98	0.98
LPE1 filter	0.98	0.94	0.98
Thermal filter type 4	0.95	0.95	0.95
LPE2 filter	0.96	0.96	0.98
Field lens	0.97	0.97	0.95
LPE2b filter	0.97	0.99	0.91
HWP	0.94	0.93	0.91
LPE2b filter	0.97	0.99	0.91
Pupil lens #1	0.97	0.96	0.97
Pupil lens #2	0.97	0.96	0.96
Polarizing grid	0.50	0.50	0.50
Camera lens	0.97	0.96	0.97
Low-pass blocker	0.96	1.00	0.96
Low-pass edge	0.86	0.95	0.96
Feed horns	1.00	1.00	1.00
Waveguides	1.00	1.00	1.00
Total	0.23	0.24	0.21

Note. These transmissions are used to determine ϵ_t in flight.

configurations, respectively. For absorption we used the optical path length of a representative detector in a given frequency band and extrapolated cryogenic loss tangent values to our temperatures (Jacob et al. 2002).

Table 5
Optical Elements Used during the Ground Measurement of Absorption Efficiency and Their Transmission for Each of the Frequency Bands

Element	150 GHz	250 GHz	410 GHz
Thermal filter type 1	1.00	0.97	0.93
Thermal filter type 2	0.97	0.96	0.90
Teflon filter	0.96	0.95	0.93
Thermal filter type 3	0.98	0.98	0.98
LPE1 filter	0.98	0.94	0.98
Thermal filter type 4	0.95	0.95	0.95
LPE2 filter	0.96	0.96	0.98
Field lens	0.96	0.97	0.95
LPE2b filter	0.97	0.99	0.91
HWP[a]	0.54	0.53	0.51
Pupil lens #1	0.97	0.95	0.96
Pupil lens #2	0.97	0.95	0.96
Grid	0.50	0.50	0.50
Camera lens	0.97	0.96	0.97
Low-pass blocker	0.96	1.00	0.96
Low-pass edge	0.86	0.95	0.96
Feed horns	1.00	1.00	1.00
Waveguides	1.00	1.00	1.00
Total	0.16	0.15	0.12

Note.
[a] At the time of this test the HWP had no antireflection coating.

The calculation of efficiencies required knowledge of the response of the instrument as a function of frequency. These measurements were reported in EP1. The bolometer efficiencies we report here are average efficiencies

$$\langle \epsilon_b \rangle = \frac{1}{\Delta\nu} \int_{\nu_1}^{\nu_2} \epsilon_b(\nu) d\nu, \quad \Delta\nu = \nu_2 - \nu_1, \tag{11}$$

where ν_1 and ν_2 define the bandwidth of the instrument $\Delta\nu$. An absorption efficiency per band is given Table 6, and the results are discussed in Section 5.4.4.

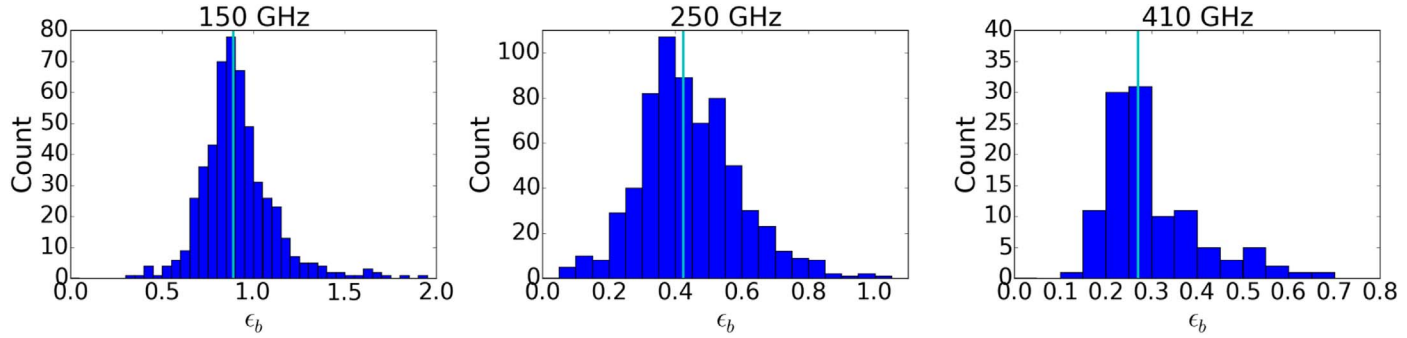

Figure 19. Average bolometer absorption efficiency distributions inferred from the calibration factors measured for all valid detectors and sections of the flight. The median efficiencies (vertical cyan lines) are given in Table 6.

Table 6
Summary of Bolometer Absorption Efficiencies per Band Extracted Using Two Different Methods

Method	150 GHz	250 GHz	410 GHz
Scans of Galactic plane	0.9	0.4	0.3
Cold load	1.0	0.3	0.2

In this section we give constraints on $\langle \epsilon_b \rangle$ using three types of measurements: (a) Galactic plane scans, (b) laboratory cold load, and (c) comparison of laboratory and in-flight optical loads. Only the laboratory cold load measurement is purely laboratory based.

5.4.1. Galactic Plane Scans

We used passes across the Galactic plane to calibrate the end-to-end response for each detector (Aubin et al. 2017). We assumed that the Galactic signal is a sum of *Planck* component maps, which have been scaled to and integrated over each of the measured bands; see the Appendix for more details. We determined the calibration factor $\mathrm{CAL} = dP_{\mathrm{inc,inst}}/dI^c$ (in units of W/count) that gave the conversion from power incident on the instrument to current flowing through a bolometer in readout system counts. We related the current in each bolometer in counts to the power absorbed using the current responsivity S_I (A/W) and the conversion from current measured in readout system counts to physical units dI_b^A/dI_b^c (A/count), which was measured in the lab and assumed to be the same for all detectors,

$$dP_{\mathrm{abs}} = dI^c \frac{dI_b^A}{dI_b^c}\frac{1}{S_I}. \tag{12}$$

Using Equations (10) and (12), the calibration factor is now

$$\mathrm{CAL} = \frac{dP_{\mathrm{inc,inst}}}{dI^c} = \frac{1}{\epsilon}\frac{dI_b^A}{dI_b^c}\frac{1}{S_I} = \frac{1}{\epsilon_t \epsilon_b}\frac{dI_b^A}{dI_b^c}\frac{1}{S_I}, \tag{13}$$

from which we find

$$\epsilon_b = \frac{1}{\mathrm{CAL}}\frac{1}{\epsilon_t}\frac{dI_b^A}{dI_b^c}\frac{1}{S_I}. \tag{14}$$

For the responsivity we assumed the slow signal limit and that the detector had large loop gain such that

$$S_I \simeq \frac{\sqrt{2}}{V_b}, \tag{15}$$

where V_b was the bolometer's known voltage bias corrected for the effects of stray impedance (Lee et al. 1998). Figure 19 shows the distributions of inferred average bolometer absorption efficiencies using the calibration factors for all sections of flight and for all detectors. (The calibration factors varied between different sections.) In Table 6 we report the median of each distribution as the absorption efficiency for the respective band. Additional discussion is given in Section 5.4.4.

5.4.2. Laboratory Cold Load

We coupled the receiver to a throughput-filling, temperature-adjustable cold load. The cold load was constructed to have an emissivity close to 1 in our frequency bands. We set the temperature of the cold load T_{cl} to several values between 25 and 50 K and at each temperature measured the electrical power necessary to operate the bolometer in transition. Similar to Equation (9), the radiative power absorbed by the bolometer in this configuration is given by

$$P_{\mathrm{abs,cl}}(T_{\mathrm{cl}}) = P_{e,d} - P_{e,\mathrm{cl}}(T_{\mathrm{cl}}) = \epsilon_b \epsilon_t P_{\mathrm{inc,cl}}(T_{\mathrm{cl}}), \tag{16}$$

where the subscript cl denotes "cold load." Note that in contrast to Equations (4) and (9) the parameterization of power in Equation (16) is in terms of the load temperature. Following the left side of the equation, we measured the absorbed radiative $P_{\mathrm{abs,cl}}$ of each bolometer by differencing the measured saturation power (from the measurement in dark conditions) and the measured electrical power in each of the cold load temperatures. This radiative load is linearly proportional to the radiative load incident on the instrument $P_{\mathrm{inc,cl}}$, which we calculated using the spectrum of a blackbody load of known temperature, the instruments' frequency bands, and the transmission efficiencies given in Table 5. The cold load measurement was done for one wafer in each frequency band.

Figure 20 shows an example of $P_{\mathrm{abs,cl}}$ as a function of the cold load temperature for one 150 GHz detector, as well as a best-fit model from which we extract its ϵ_b. The figure also shows the distribution of derived bolometer absorption efficiencies for each frequency band. The medians of the distributions are reported in Table 6. Additional discussion is given in Section 5.4.4.

5.4.3. Comparison of Laboratory and In-flight Optical Loads

A combination of Equations (9) and (10) gives

$$P_{\mathrm{abs},f} = \epsilon_t \epsilon_b P_{\mathrm{inc,inst},f} = P_{e,d}(T_0) - P_{e,f}(T_0), \tag{17}$$

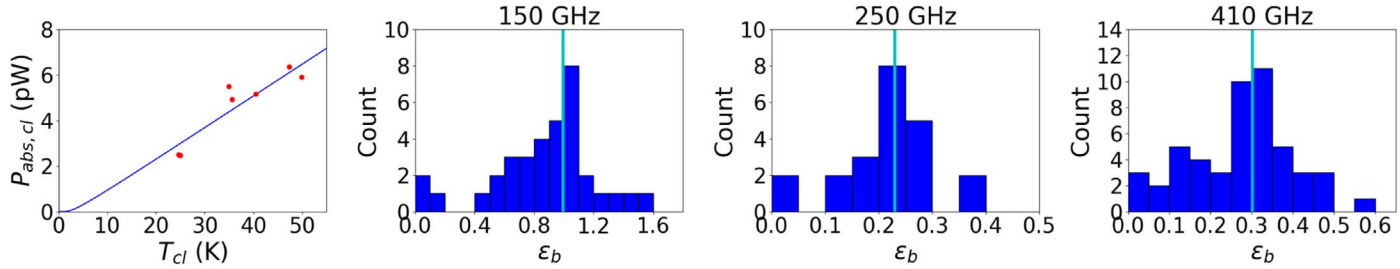

Figure 20. Left: measured (red circles) and fitted (solid blue) power absorbed by a 150 GHz bolometer as a function of the cold load temperature. Right: distribution of measured bolometer absorption efficiency and their median (vertical cyan lines) for each of the frequency bands. The median values are given in Table 6.

Table 7
Predicted Optical Power Incident on the Bolometer during Flight $P_{\rm inc,f}$

Element	150 GHz (pW)	250 GHz (pW)	410 GHz (pW)
CMB	0.063	0.032	0.0047
Atmosphere	0.0054	0.064	0.37
Mirrors	0.19	0.45	0.76
Instrument	0.36	1.3	3.5
Total	0.62	1.8	4.7

Note. For each element the power incident on the instrument is higher and is reduced by reflection and absorption by optical elements along the light path. Emission by the instrument is dominated by a half-inch-thick Teflon filter that had a temperature of 110 K and by the HWP that reached ∼50 K.

where $P_{\rm inc,inst,f}$ is the radiative power incident on the instrument in flight. We find

$$\epsilon_b = \frac{P_{e,d}(T_0) - P_{e,f}(T_0)}{\epsilon_t P_{\rm inc,inst,f}} = \frac{P_{e,d}(T_0) - P_{e,f}(T_0)}{P_{\rm inc,f}}, \quad (18)$$

where $P_{\rm inc,f}$ is the radiative power incident on the bolometer in flight.

We calculated the power incident on the detectors by including contributions from the sky (CMB and atmospheric emission; Bao 2015), the mirrors, other optical elements along the optical path, such as the vacuum window and absorptive filters, and the transmission coefficients listed in Table 4 (Aubin 2012); see Table 7. The electrical powers in Equation (18) were known from laboratory and in-flight load curve measurements (see Section 5.3). We found median bolometer absorption efficiencies of 3.4, 1.1, and 0.7 for the 150, 250, and 410 GHz bands, respectively. Bolometer absorption efficiencies larger than 1 are unphysical, and we discuss this result in the next section.

5.4.4. Discussion of Absorption Efficiency Results

The calibration and cold load measurements give approximately consistent results: a relatively high absorption efficiency at the 150 GHz band and medium absorption at the 250 and 410 GHz bands. The calibration measurement is based on the response to changes in the signal level as the instrument passes across the Galactic plane. The scatter in the histograms of Figure 19, which gives some values that are larger than 1, is due primarily to larger uncertainty in the Galactic calibration for some of the detectors. The other two measurements are sensitive to the total power absorbed in the detector. The cold load measurement also has some scatter due to noise or systematic errors in the calculation of the absorbed power. For example, it is sometimes challenging to accurately estimate P_e from the load curves such as shown in Figure 17.

The results giving absorption efficiencies larger than 1 for the load-curve-based measurement indicate that the denominator in Equation (18) had been underestimated and that there was excess load that was not accounted for by the sources listed in Table 7. To find the magnitude of the excess absorbed load, we difference the measured and expected values. The measured loads are 3.6, 5.3, and 5.0 pW for the 150, 250, and 410 GHz bands, respectively; see Section 5.3. The expected absorbed load is inferred from the product of the expected load incident on the bolometer, as given in Table 7, and the bolometer absorption efficiencies coming from the Galaxy calibration; see Table 6. We find excess absorbed load of 3.1, 4.6, and 3.6 pW for the 150, 250, and 410 bands, respectively. These excess loads were not observed with the laboratory cold load. We note that the design values for the thermal conductances were based on power saturation values of 4, 9, and 12 pW, respectively; see Section 5.1.2. Relative to our pre-instrument construction estimates, we find a reduction in sky signal and an increase in instrumentally induced load that give a total load consistent with our margin of safety. The reduction in sky signal was a result of having bands with transmission that was approximately half that expected relative to top-hat bands with the same edges.

We hypothesize that beam spillover past the vacuum window and onto warm surfaces outside of the receiver—here we view the beam as emanating from the focal plane toward the sky—gave rise to the excess load. This spillover was not detected with the cold load because the load was mounted onto the vacuum window flange and therefore intercepted the entire throughput.

5.5. Noise Performance

We used flight data to quantify individual-detector and overall instrument noise and compare it to expectations. The NEP N, which for brevity we also refer to as "noise," consists of several terms:

$$\begin{aligned} N\ (\mathrm{W}/\sqrt{\mathrm{Hz}}) &= [N^2_{\rm photon} + N^2_{\rm phonon} + N^2_{\rm Johnson} + N^2_{\rm readout}]^{1/2} \\ &= \left[\left(2h\nu P_{\rm abs} + \xi\frac{P^2_{\rm abs}}{\Delta\nu}\right) + \gamma 4k_B T^2 G \right. \\ &\quad \left. + \frac{1}{S_I^2}\cdot\frac{4k_{\rm B}T}{R} + \frac{1}{S_I^2}\cdot N^2_{\rm readout}\right]^{1/2}, \end{aligned} \quad (19)$$

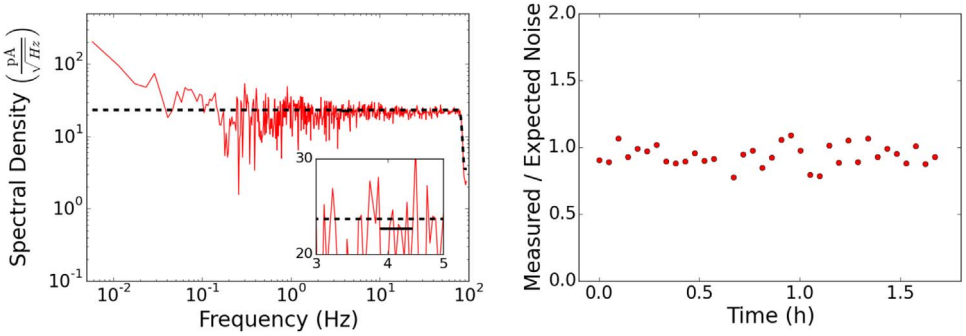

Figure 21. Left: current spectral density of one 150 GHz detector during one 172 s section of the flight when it was overbiased (solid red line), with a detailed view of the data between 3 and 5 Hz (inset). The expected quadrature sum of the Johnson and readout noise (dashed black line) is within 10% of the measured noise level averaged over a narrow band from 3.9 to 4.4 Hz (solid black line). Right: measured-to-expected readout and Johnson noise ratio as a function of time for the same detector.

where h is Planck's constant, ν is the center of the observation frequency band, ξ is a unitless number between zero and one quantifying the photon correlation, γ is a unitless number between zero and one accounting for the temperature gradient along the link from the TES to the bath, k_B is Boltzmann's constant, T is the TES temperature, and R is the TES resistance (Mather 1982).

TOD from flight is used to directly assess N, that is, the left side of Equation (19). We used several configurations to assess the contributions of specific terms on the right-hand side of Equation (19). For each configuration we compared the measurement to expectations. We then combined the contributions in quadrature and compared to the total measured noise N. We determined the combination of $N_{\rm Johnson}$ and $N_{\rm readout}$ using measurements when the detectors were biased above their superconducting transition, $N_{\rm phonon}$ using the measured thermal conductances and critical temperatures, and $N_{\rm photon}$ using the measured radiative load.

To assess any noise contribution X using flight data, we divided the data into segments of 172 s length and made use of all possible segments. Momentary glitches such as cosmic-ray hits were replaced with white-noise realizations. Sections of data that had more than 10% of their samples flagged as glitches were excluded from the analysis. For each section we removed an offset and a gradient, applied a Hann window, and calculated the spectral density. For the assessment of the readout and Johnson noise, the data were converted from raw digital units (counts) to current referred to the SQUID input (A) using Equation (1). For the assessment of the total NEP, these data were converted from current through the SQUID to power absorbed at the detector by applying the current responsivity S_I,

$$X\ [\mathrm{W}/\sqrt{\mathrm{Hz}}] = \frac{X\ [\mathrm{counts}/\sqrt{\mathrm{Hz}}] \cdot dI_b^A/dI_b^c\,[\mathrm{A/count}]}{S_I\,[\mathrm{A/W}]}. \tag{20}$$

For each section of data we find the mean level of the spectral density between 3.9 and 4.4 Hz, which is one of the polarization frequency sidebands.

5.5.1. Johnson and Readout Noise

When the detectors were biased above their superconducting transition—we will use the shorthand "overbiased"—the current responsivity was low and the last two terms in Equation (19) should dominate the overall noise. The spectral density for one section of such data for one detector is shown in the left panel of Figure 21. The measurement is shown in units of $\mathrm{A}/\sqrt{\mathrm{Hz}}$ following Equation (1) since both $N_{\rm readout}$ and $N_{\rm Johnson}$ are intrinsically current noise sources. To assess noise level over time, we calculated such spectral density for all valid sections over 1.7 hr of data, about 35 sections per detector. We find that within ~20% the noise levels recorded are stable; see the right panel of Figure 21. Higher variations are expected as compared to the resistor case in Section 4.3 since overbiased detectors have residual sensitivity to stage temperature variations and incident power.

For each detector we calculated the predicted readout noise using the electronic specifications of each element of the readout chain (Aubin 2012). To estimate the Johnson noise, we assumed a detector resistance R_n as inferred from the network analysis and a detector temperature $T = T_c + \Delta P/\overline{G}$, where ΔP is the difference between the electrical power dissipated when the detector is overbiased and $P_{\rm sat}$ measured in dark conditions. We added the predicted contributions from readout and Johnson in quadrature to find a combined noise term (in $\mathrm{A}/\sqrt{\mathrm{Hz}}$). We multiplied this term by a factor of 1.7. This is the factor that accounts for the excess noise that was observed with the resistor measurements described in Section 4.3.1. The expected levels shown in Figures 21 and 22 include this extra factor. For each detector and for all sections over the given 1.7 hr of data we formed the ratio of measured to expected noise and found the median. A histogram of the medians for all detectors is shown in Figure 22. Table 8 gives the median ratios for each wafer. The median ratio for all detectors is 1.0.

There was excess noise identified with resistor channels in Section 4.3, amounting to a factor of 1.7 higher than predictions. When this excess is added to predictions of bolometer noise in the overbias state, we find consistency with measurements. We noted in Section 4.3.1 that noise measurements in the overbias state after the North American engineering flight did not exhibit this excess noise. The ratio of measured to predicted noise was 1.0 ± 0.1 (Aubin et al. 2010). These measurements were done in the flight receiver, but the receiver was in the laboratory, without other EMI sources such as attitude control motors and telemetry transmitters. We therefore hypothesize that EMI contributed additional noise that is most apparent in configurations in which the Johnson and readout noise terms dominate.

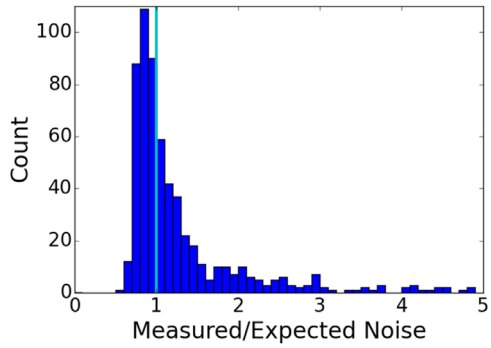

Figure 22. Histogram of the median ratio of measured to expected readout and Johnson noise for all bolometers. There are 68 bolometers (not shown) with a ratio greater than 5. The median value (vertical cyan) is 1.0, and the mode is centered at 0.85.

Table 8
The Expected Combination of Johnson and Readout Noise and the Ratio of Measured to Expected Levels as Measured in Flight for Overbiased Detectors

Wafer	Expectation ($pA/\sqrt{Hz}$)	Measured/Expected Ratio
150-09	20	1.1
150-14	18	1.3
150-15	18	0.9
150-39	22	0.8
150-43	24	1.0
150-47	24	1.0
250-23	22	1.0
250-24	26	0.9
250-29	21	1.2
410-28	32	1.0
All detectors		1.0

Note. For each wafer the ratio is for the median of the distribution for the detectors on that wafer. The first three digits for the wafer number give its operating frequency band.

5.5.2. Noise-equivalent Power in Transition

The total noise N when the detector operates in its superconducting transition is given by Equation (19). We report on measured N using flight data after removal of the HWPSS (see Section 3). We used all the data that passed quality cuts to be used for astrophysical analysis but also included additional data that would otherwise not be used because of, for example, large pointing errors or scan speeds that were too low.

The NEP as a function of time throughout flight for one 150 GHz detector is shown in Figure 23, along with the expected value. We describe the calculation of the expected value in the next paragraph. As before, we found a representative value for the ratio of measured to expected NEP throughout flight for a given detector by finding the median over all sections. We combined the medians for each detector to find a median per wafer, which is reported in Table 9. A median measured NEP per frequency band is given in Table 10. Figure 23 gives a histogram for the medians of measured-to-expected ratio for all detectors.

We calculated an expected NEP by finding the theoretical Johnson and readout current noise terms and multiplying them by (1) a factor of 1.7 coming from the excess noise in the resistor measurements (see Section 4.3.1) and (2) an additional factor per wafer as listed in Table 8. The second factor has been identified through the noise measurement with overbiased detectors (see Section 5.5.1). To convert from current noise to NEP, we divided the Johnson and readout noise terms by the current responsivity and assumed the high loop-gain limit. We assumed $\gamma = 0.5$ to predict the phonon noise (Mather 1982). We calculated photon noise using the measured radiative load per detector, as described in Section 5.3. We quote the predicted level for a photon correlation factor of 1. The median predictions decrease by 20% (7%) when using a correlation factor of 0 for the 150 and 250 (410) GHz bands.

For the 150 band the measured noise is broadly consistent with calculations after accounting for the excess noise identified through measurements with resistors. No further excess noise is identified when operating the bolometers in transition. The average noise increase for the three (one) wafers at 250 (410) GHz is about 30% (60%) after accounting for the excess noise. This level is at the border or beyond the 20%–30% uncertainties in our estimates. This additional source of noise is being investigated, although the small number of available wafers may give a biased impression of trends.

6. Noise-equivalent Temperature and Map Depth

We estimated the NET in two ways: (1) using the TOD in counts and the calibration factors that convert count to temperature, and (2) converting the measured NEP to NET. The term "temperature" refers to equivalent sky CMB temperature fluctuations. In this section we describe the two methods and show that they give consistent results. We then use the measured NET and the instantaneous attitude information to produce depth maps for each of the frequency bands.

6.1. NET Using the TOD and Calibration

For each detector we calculated power spectral densities of 5.7-minute sections of calibrated, deglitched, HWPSS-subtracted TOD and fit them with a three-parameter noise model $M(f)$ consisting of red- and white-noise terms as a function of frequency,

$$M(f) = W^2\left[1 + \left(\frac{f_k}{f}\right)^{\alpha}\right]. \quad (21)$$

The parameters are W^2, the white-noise level (in K^2/Hz); f_k, the frequency cutoff of the red-noise power law (also referred to as f_{knee}, in Hz); and α, the red-noise spectral index. We used all calibrated data throughout flight that passed quality cuts for astrophysical analysis (see Didier 2016) and added other data with valid noise information but that would not pass cuts for making maps. Such data included sections during times at which the attitude reconstruction was poor or the scan speeds were below or above specific thresholds. A polynomial with up to cubic terms in time was subtracted from the TOD before applying a Hann window and calculating the PSD. Figure 24 shows an example of a PSD and its model fit for one section of the data of a 250 GHz detector.

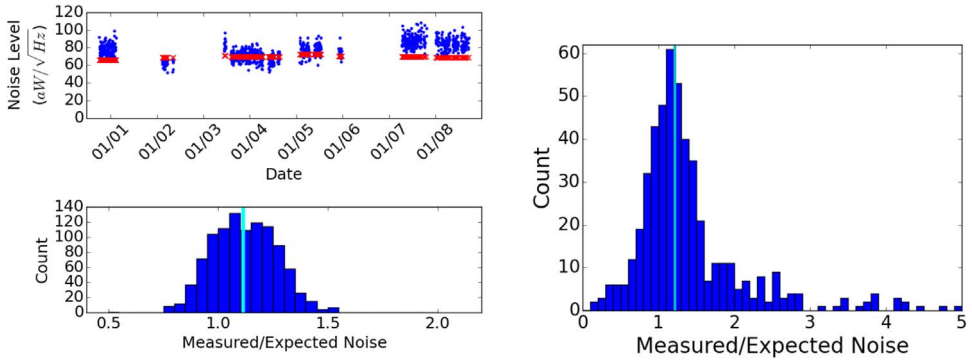

Figure 23. Top left: in-transition measured (blue circles) and expected (red crosses) NEP for one 150 GHz detector throughout flight. Gaps indicate times when data are absent or rejected. Bottom left: distribution of measured-to-expected ratio for this detector throughout flight, and the median (vertical cyan) ratio of 1.1. Right: distribution of the median ratio of measured to expected in-transition noise throughout flight for all bolometers. The median ratio (vertical cyan) is 1.2.

Table 9
The Median Expected NEP and Measured-to-expected Ratio for Each Wafer and Combined for All Detectors

Wafer	Expected NEP [aW/$\sqrt{\text{Hz}}$]	Measured/Expected Ratio
150-09	69	1.1
150-14	48	0.7
150-15	57	1.1
150-39	77	1.1
150-43	56	1.2
150-47	64	1.3
250-23	92	1.1
250-24	78	1.4
250-29	98	1.4
410-28	103	1.6
All detectors		1.2

Table 10
The Median NEP Contributions to Noise Measured in Transition for Each Frequency Band

Noise source	Value ($aW/\sqrt{\text{Hz}}$)		
	150 GHz	250 GHz	410 GHz
Readout	$\sqrt{2}\cdot 15$	$\sqrt{2}\cdot 15$	$\sqrt{2}\cdot 23$
Johnson	$\sqrt{2}\cdot 7.6$	$\sqrt{2}\cdot 8.2$	$\sqrt{2}\cdot 13$
Phonon	22	25	32
Photon	32	49	63
Excess	43	64	133
Total	62	88	160

The fitting—conducted on at least 10 sections of data for each detector, but typically over many hours of data—generated a set of parameters W, f_k, and α, with which we characterized the noise performance. For each detector we find the three median parameter values over all flight. We histogram

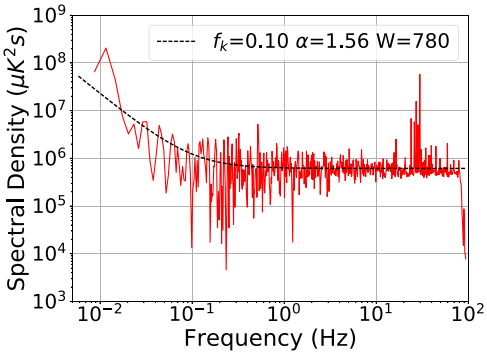

Figure 24. Example PSD (solid red line) for one section of a 250 GHz bolometer data with a fit (dashed black line) to the noise model of Equation (21).

these median values for all available detectors per frequency band in Figures 25–27. The figures also give the medians of the distributions.

The data show knee frequencies near 200 mHz and red-noise power-law index near 2.3. These relatively high values are not intrinsic to the detectors or readout, but rather are a consequence of the azimuth motor malfunction, described in EP3. In the absence of controlled azimuth pointing, the payload executed full rotations, causing strong Sun-synchronous drifts in the TOD. Removal of a cubic-order polynomial from the TOD removes some of the drifts, but remnants are manifest in the statistics of f_k and α. A correlation analysis between the noise properties of different detectors showed strong coherency at low frequencies supporting the model of drifts due to Sun-synchronous signals.

6.2. NET Using the NEP

We converted the measured NEP to NET using

$$\text{NET}(\mu\text{K}\sqrt{\text{s}}) = \text{NEP}(\text{W}/\sqrt{\text{Hz}})\left(\frac{dT}{dP}\right)\Big|_{T_{\text{CMB}}}\frac{1}{\sqrt{2}}, \qquad (22)$$

where $\left(\frac{dT}{dP}\right)\Big|_{T_{\text{CMB}}}$ is a conversion factor from absorbed power to temperature calculated using the throughput, measured bands, and efficiency. For NEP we used the median calculated for all detectors in a given frequency, as listed in Table 11.

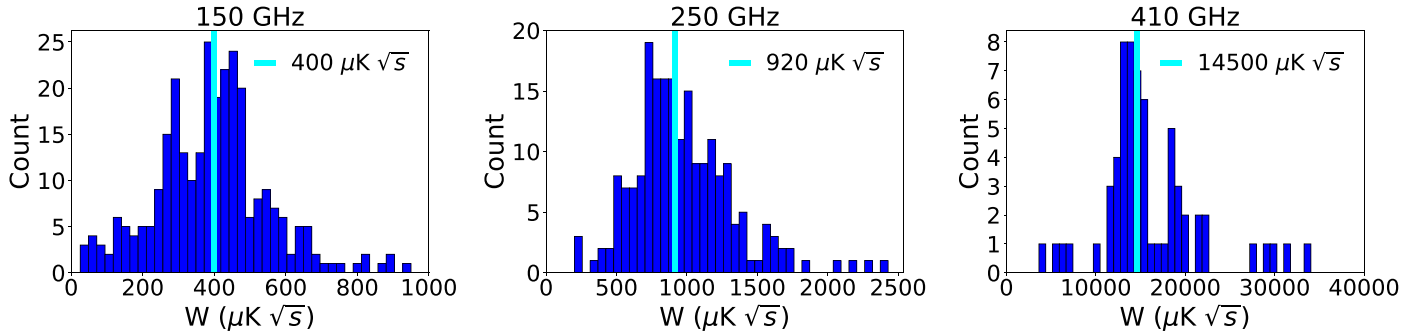

Figure 25. Distribution of median NET for all available detectors in a given frequency band and the median of the distribution (vertical cyan lines).

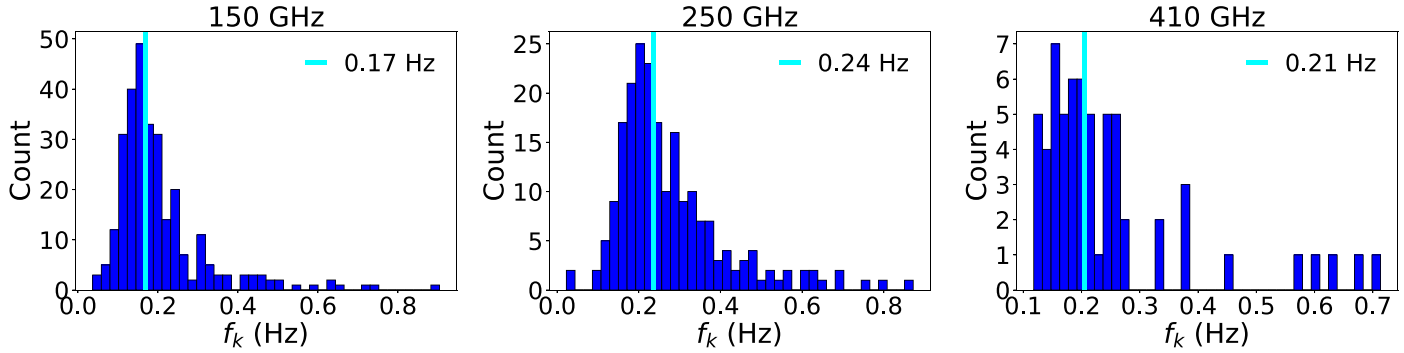

Figure 26. Distribution of median knee frequencies for all available detectors in a given frequency band and the median of the distribution (vertical cyan lines).

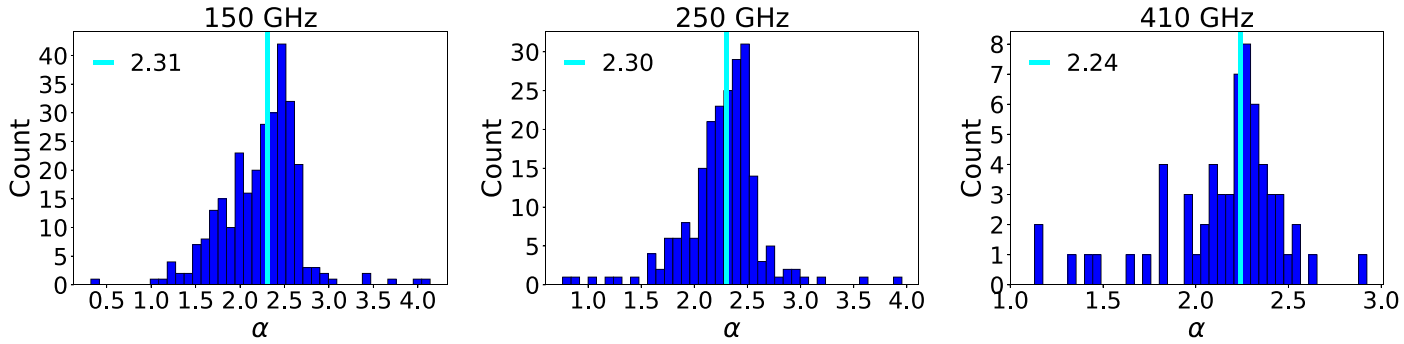

Figure 27. Distribution of median red-noise power-law indices for all available detectors in a given frequency band and the median of the distribution (vertical cyan lines).

6.3. Discussion of NET

The two approaches for finding the NET are not independent. Finding NET using the measured calibration factors makes no assumption about the instrument's transmission efficiency and specific detector absorption efficiency. Finding NET using the NEP does not explicitly depend on the measured calibration factors. However, the conversion from *absorbed* power to temperature *on the sky*, as given in Equation (22), depends on the transmission and absorption efficiencies, which were derived—at least in one way of finding efficiencies—using the calibration factors. Therefore, the comparison we are providing is a check on end-to-end consistency, rather than a comparison of results using two entirely independent methods.

The measured NETs are consistent within 10% for the 150 and 250 GHz bands. There is a larger difference for the 410 GHz band. The estimate from the NEP depends on the product of the instrument's throughput and efficiency through the multiplicative factor *dT/dP*; see Equation (22). For the throughput we assumed a single mode ($A\Omega = \lambda^2$) for the propagating electromagnetic wave. We hypothesize that at the highest-frequency band we are underestimating the throughput by assuming a complete cutoff of the second mode. A 25% higher throughput brings the NET from NEP and NET from calibration to values that agree within our overall uncertainty.

Table 11
The Median Measured NEP per Frequency Band and Comparison of NET Calculated from the NEP Using the Measured Efficiency, Frequency Bands and Assumed Throughput, and the NET Measured Using the Calibration

	150 GHz	250 GHz	410 GHz
NEP (aW/$\sqrt{\text{Hz}}$)	62	88	160
NET from NEP (μK $\sqrt{\text{s}}$)	380	1000	23000
NET from calibration (μK $\sqrt{\text{s}}$)	400	920	14500

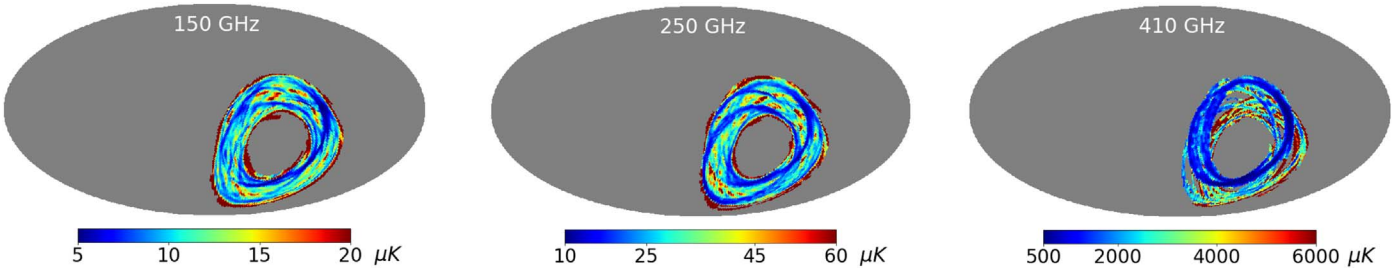

Figure 28. Depth maps in Galactic coordinates using the NET and attitude reconstruction from the EBEX2013 flight. The maps use HEALPix $N_{\rm side} = 64$ pixels, and the color scale is linear. At this pixelization the median pixel noise is 11, 28, and 1982 μK for the 150, 250, and 410 GHz bands, respectively.

6.4. Map Depth

The high-fidelity attitude reconstruction from the EBEX2013 flight was discussed in EP3. We binned all the data that passed quality cuts for making maps using HEALPix (Górski et al. 2005) with $N_{\rm side} = 64$. With each sample we associated an equivalent temperature noise N_s (in μK) equal to the product of the NET calculated during that time section and the square root of the sampling rate. We calculated depth per pixel D_p following

$$D_p = \left(\sum \frac{1}{N_{s,p}^2}\right)^{-1/2}, \quad (23)$$

where the sum is over all samples that had pointing associated with a given pixel p.

The depth maps with pixels of $\sim$1 deg^2 for the three frequency bands are shown in Figure 28. The noise distribution is strongly inhomogeneous, a consequence of an azimuth motor malfunction, as described in EP3. The median depth values per pixel for the 150 and 250 GHz bands—11 and 28 μK, respectively—are several factors larger than those reported by *Planck* and the expected CMB *E*-mode signal. A signal-to-noise ratio above 1 is only achieved for a fraction of the pixels on the Galaxy at 410 GHz. The depth maps do not encode $1/f$ noise and filtering that further degrades the signal-to-noise ratio. We therefore decided not to publish maps.

7. Summary

EBEX was a CMB polarimeter that had two focal planes consisting of 14 detector wafers. Each focal plane had four wafers operating at 150 GHz, two at 250 GHz, and a central wafer at 410 GHz. We have presented the design of bolometers optimized for the low optical load in the stratosphere and for operation at 410 GHz, a frequency that is unique for balloon payloads. To handle the thin wafers suitable for this frequency band, we have developed a technique to bond them to thicker wafers. We have shown distributions of measured thermal conductances, normal resistances, transition temperatures, and time constants. For the 250 and 410 GHz bands the median thermal conductances were within 20% of design values. For the 150 GHz band, for which our target was 2.4 times lower than for the 250 GHz band, the median measured value was 2 times higher than design. This result reflects the additional challenge in making very low thermal conductance spider-web bolometers operating at 0.25 K. The lower thermal conductance is a consequence of the lower optical load expected at 150 GHz; see Table 7. The measured transition temperatures were within 10% of design values, and median measured (design) saturation powers were 7.8 (4), 12 (9), and 14 (12) pW for the 150, 250, and 410 GHz bands, respectively. The measured time constants were 3.5–5.7 times longer than design values. Either published values for specific heats of the materials that made up the bolometer are incorrect, or the devices had been contaminated by unknown materials during fabrication.

We have measured in-flight median optical loads of 3.6, 5.3, and 5.0 pW at 150, 250, and 410 GHz, respectively. Given the final configuration of all optical elements inside the instrument and the measured frequency bands, we have calculated the expected contributions from the sky, warm telescope, and instrument emission. The warm mirrors, a Teflon filter, and the HWP dominated the expected load. We have also identified excess optical load in flight, but no excess load was measured when we coupled a 4 K load onto the vacuum window of the receiver in the laboratory. We therefore attribute the additional load to spillover of throughput onto warm surfaces outside of the receiver.

Two measurement methods for finding the bolometer absorption efficiencies gave consistent results within 10% for all frequency bands. They indicate high absorption efficiency ($\sim$0.9) for the 150 GHz and medium (medians of $\sim$0.35 and $\sim$0.25) for the 250 and 410 GHz bands. The measured distributions are broad, occasionally giving apparently unphysical absorption values larger than 1. However, noisy measurements that give wide distributions can give values larger than 1.

EBEX was the first experiment to implement the digital version of an FDM system aboard a balloon payload. For several years it had the highest multiplexing factor of 16 until SPT3G began implementing a multiplexing factor of 64 in 2016. We have developed novel, superconducting, low-inductance microstrips. We have measured gain stability of better than 0.25% over 13 hr and better than 2% over the duration of the flight, even as the temperature of the readout boards experienced temperature excursions of up to 20°C.

The rotation of the HWP introduced an HWP synchronous signal in the TOD. To assess the noise performance, we have fit and removed the synchronous signal. We have given a detailed accounting of the measured noise. The readout noise was measured to match predictions in the laboratory and for dark SQUIDs in flight. We have found excess noise in flight when analyzing resistor data and when the detectors were in an overbiased state, for which the readout noise and Johnson noise are expected to be dominant. The median excess noise was a factor of 1.7 larger than the expected total of Johnson and readout noise terms. When we included an extra noise term to account for the excess noise observed in the overbias state, the median measured noise in transition was 20% higher than expectation. We suspect that electromagnetic pickup from

telemetry electronics coupling to the long microstrips was the cause for the excess noise.

We have calculated the median NET in two ways and found consistency for the 150 and 250 GHz bands. The preflight expectation for 150 GHz, taking into account the high thermal conductivity detectors, but without excess noise or load, was 210 μK $\sqrt{\text{s}}$. For the target thermal conductivity of 19 pW/K, the expectation was 180 μK $\sqrt{\text{s}}$, a factor of 2.2 lower than the achieved value of 400 μK $\sqrt{\text{s}}$. Our expectation of 180 μK $\sqrt{\text{s}}$ was higher by a factor of 1.3 compared to the best reported by BOOMERANG (which also had bolometers operated at a bath temperature near 0.25 K; Crill et al. 2003) because EBEX had two warm mirrors, not one, higher internal emission from a Teflon filter due to a much larger vacuum window, higher temperature for its rotating HWP, and higher detector thermal conductivity than required at 150 GHz. We chose high detector thermal conductance because it mitigated the risk of unanticipated optical load at the expense of higher noise. This choice proved prudent; we did experience excess load but continued to operate the majority of the bolometers. A next-generation balloon-borne instrument that has only one ambient temperature mirror, has detectors with appropriately low thermal conductivity, and applies the lessons learned from EBEX2013 (including having lower internal emission from filters and HWP, and mitigating excess load and noise) can achieve 140 μK $\sqrt{\text{s}}$ at 150 GHz.

EBEX was the first balloon experiment to implement a kilopixel array of bolometers in the focal plane. It was among the first to face the challenges imposed by a significantly larger focal plane, optical elements, and a vacuum window. The EBEX experience suggests the following path for a future experiment with kilopixel TES arrays to make optimal use of the balloon environment. (1) Reduce instrument emissions through the development and implementation of high thermal conductance, through low millimeter-wave emissivity and reflectivity IR filters and lenses, and by maintaining optical elements at cold temperatures if practical. However, for an experiment that targets a resolution finer than $\sim 25'$ at 150 GHz, at least one reflector will almost certainly still need to be maintained at ambient temperatures. (2) Implement optical elements that are appreciably larger than the nominal optical bundle to mitigate diffraction near apertures and thus reduce spillover outside the designated throughput, even at the expense of a larger cryostat, larger window, and potentially heavier payload. (3) Pay attention to EMI mitigation, as wiring that couples the SQUIDs to the detector focal plane is susceptible to the transmitter-heavy environment on board the payload. (Since the EBEX2013 flight there have been additional reports of excess noise due to telemetry electronics in other millimeter and submillimeter experiments; Galitzki et al. 2014; Gambrel 2018.) The EMI integrity of the wiring cavity of the cryostat should be excellent, or experiments should impose radio silence after initial checkup and calibration. Significant time should be allocated to testing in full flight configuration, including telemetry electronics.

Because of the malfunction of the azimuth motor, a result of thermal design error that is discussed in EP3, the instrument scanned $\sim 6000\,\text{deg}^2$, giving shallow depth with highly inhomogeneous noise. We have presented depth maps that gave a median noise of 11 and 28 μK per HEALPix ($N_{\text{side}} = 64$) pixel at 150 and 250 GHz. The map noise is higher compared to *Planck*'s noise, as well as to that of other contemporaneous experiments, and we did not find it compelling to publish our own maps or power spectra.

EBEX pioneered the use of TES bolometers on a balloon-borne platform. It was the first experiment to fly a small array of these detectors in a test flight in 2009 and a kilopixel array during its EBEX2013 flight. Nearly 1000 bolometers were operating shortly after the payload reached float altitude. EBEX pioneered the use of the digital FDM readout system. This system is now implemented on several operating ground-based instruments (Benson et al. 2014; Inoue et al. 2016; Stebor et al. 2016) and is baselined for a proposed space mission (Suzuki et al. 2018). EBEX was also the first astrophysics experiment to implement an SMB. This system is also baselined for a ground-based and a proposed space mission (Iida et al. 2017; Hill et al. 2018). EBEX was a successful technology pathfinder for future CMB space missions.

Support for the development and flight of the EBEX instrument was provided by NASA grants NNX12AD50G, NNX13AE49G, NNX08AG40G, and NNG05GE62G and by NSF grants AST-0705134 and ANT-0944513. We acknowledge support from the Italian INFN INDARK Initiative. P.A. and G.S.T. acknowledge the Science & Technology Facilities Council for its continued support of the underpinning technology for filter and wave plate development. We also acknowledge support by the Canada Space Agency, the Canada Research Chairs Program, the Natural Sciences and Engineering Research Council of Canada, the Canadian Institute for Advanced Research, the Minnesota Supercomputing Institute, the National Energy Research Scientific Computing Center, the Minnesota and Rhode Island Space Grant Consortia, our collaborating institutions, and Sigma Xi, The Scientific Research Society. Research described in this paper used facilities of the Midwest Nano Infrastructure Corridor (MINIC), a part of the National Nanotechnology Coordinated Infrastructure (NNCI) program of the National Science Foundation. C.B. acknowledges support from the RADIO-FOREGROUNDS grant of the European Union's Horizon 2020 research and innovation program (COMPET-05-2015, grant agreement no. 687312). J.D. acknowledges a NASA NESSF fellowship NNX11AL15H. B.R.-K. acknowledges an NSF Post-Doctoral Fellowship AST-1102774 and a NASA Graduate Student Research Fellowship. K.R. and K.Z. acknowledge support by the Minnesota Space Grant Consortium. The Flatiron Institute is supported by the Simons Foundation. S.M.F. was partially supported by the UK Science and Technology Facilities Council (STFC). We very much thank Danny Ball and his colleagues at the Columbia Scientific Balloon Facility for their dedicated support of the EBEX program. We thank Darcy Baron and Kaori Hattori for inputs on the stray inductance of the microstrips and an anonymous referee for his/her careful and thoughtful review.

Appendix
Calibration

The calibration produces two equivalent conversions, one from measured counts to signal power incident on the instrument, and the other from measured counts to CMB temperature fluctuation of magnitude K_{CMB}. In Section 5.4.1 we use CAL, which is the conversion from counts to power: $\text{CAL} = dP_{\text{inc,inst}}/dI^c$ (W/count). For completeness, for the purpose of this appendix, we denote as CAL_T the quantity

$\mathrm{CAL}_T = dT_{\mathrm{inc,inst}}/dI^c$ (K/count), where T_{inc} refers to CMB temperature fluctuation of magnitude T_{inc} (K). To find these calibration factors using passes across the Galactic plane, we build reference signal maps at our frequency bands from the *Planck* component maps described in Planck Collaboration et al. (2016). We use the R2 *Planck* component maps processed with the Commander framework from https://pla.esac.esa.int/#maps. The reference signal maps are a combination of thermal dust, free–free, CO, and the CMB. Within the EBEX bands and near the Galactic plane the maps are entirely dominated by the dust component.

We now describe the making of the dust intensity map as a function of frequency. Other signal maps, corresponding to other components, are made in the same way using the extrapolation factors provided in Planck Collaboration et al. (2016). The thermal dust amplitude map A_D referred to a baseline frequency $\nu_{0D} = 545$ GHz is first converted from its native K_{RJ} units to intensity ($\mathrm{W/sr\,m^2\,Hz}$). The resulting map is then extrapolated to frequency ν using the frequency scaling factor

$$\left(\frac{e^{\frac{h\nu_{0D}}{kT_D}}-1}{e^{\frac{h\nu}{kT_D}}-1}\right)\left(\frac{\nu}{\nu_0}\right)^{\beta_D+3} \tag{24}$$

and using the *Planck*-provided maps of dust temperature T_D and spectral index β_{D}.

The total incident signal map (at each frequency) is a sum of the individual component signal maps. To find the total incident signal power, we integrate the total incident reference signal map over the EBEX bands (as measured and reported in EP1) and multiply by the throughput of the instrument. A linear regression of the power in the reference map versus counts measured by a given bolometer when passing the galactic plane gives CAL for that bolometer.

The total incident signal map (at each frequency) is alternatively converted to K_{CMB} using the spectral radiance of a blackbody $B_\nu(\nu, T)$. It is then integrated as a function of frequency and weighted by the normalized transmission of the instrument. A linear regression of the temperatures in the reference map to the counts measured by a given bolometer when passing the Galactic plane give CAL_T for that bolometer.

ORCID iDs

Maximilian Abitbol https://orcid.org/0000-0001-8071-6735
Peter Ade https://orcid.org/0000-0002-5127-0401
Derek Araujo https://orcid.org/0000-0003-0527-2948
François Aubin https://orcid.org/0000-0002-8241-4156
Joy Didier https://orcid.org/0000-0003-4151-9450
Shaul Hanany https://orcid.org/0000-0002-8702-6291
Kyle Helson https://orcid.org/0000-0001-9238-4918
Andrew Jaffe https://orcid.org/0000-0003-2086-1759
Lorne Levinson https://orcid.org/0000-0003-4679-0485
Michele Limon https://orcid.org/0000-0002-5900-2698
Ilan Sagiv https://orcid.org/0000-0001-8377-3153
Gregory S. Tucker https://orcid.org/0000-0002-6954-6947
Karl Young https://orcid.org/0000-0002-1337-6088
Kyle Zilic https://orcid.org/0000-0003-1971-7151

References

Ade, P., Akiba, Y., Anthony, A., et al. 2014, ApJ, 794, 171
Araujo, D. 2017, PhD thesis, Columbia Univ.
Aubin, F. 2012, PhD thesis, McGill Univ.
Aubin, F., Aboobaker, A. M., Ade, P., et al. 2010, Proc. SPIE, 7741, 77411T
Aubin, F., Aboobaker, A. M., Bao, C., et al. 2017, in The Fourteenth Marcel Grossmann Meeting, ed. M. Bianchi (Singapore: World Scientific Publishing Co.), 2084
Bao, C. 2015, PhD thesis, Univ. Minnesota
Baumann, D., Jackson, M. G., Adshead, P., et al. 2009, in AIP Conf. 1141, CMB Polarization Workshop: Theory and Foregrounds, ed. S. Dodelson et al. (Melville, NY: AIP), 10
Benson, B. A., Ade, P. A. R., Ahmed, Z., et al. 2014, Proc. SPIE, 9153, 9153
BICEP2 Collaboration, Ade, P. A. R., Aikin, R. W., et al. 2014, PhRvL, 112, 241101
BICEP2/Keck and Planck Collaborations, Ade, P. A. R., Aghanim, N., et al. 2015, PhRvL, 114, 101301
Bock, J. J., Chen, D., Mauskopf, P. D., & Lange, A. E. 1995, SSRv, 74, 229
Chang, C. L., Ade, P. A. R., Aird, K. A., et al. 2009, in AIP Conf. Proc. 1185, The 13th International Workshop on Low Temperature Detectors (Melville, NY: AIP), 475
Chapman, D. 2015, PhD thesis, Columbia Univ.
Chapman, D., Aboobaker, A. M., Araujo, D., et al. 2015, in IEEE Aerospace Conf., 7119013
Chapman, D., Didier, J., Hanany, S., et al. 2014, Proc. SPIE, 9152, 915212
Crill, B. P., Ade, P. A. R., Artusa, D. R., et al. 2003, ApJS, 148, 527
Didier, J. 2016, PhD thesis, Columbia Univ.
Didier, J., Chapman, D., Aboobaker, A., et al. 2015, in Proc. IEEE Aerospace Conf., 7119010
Didier, J., Miller, A., Araujo, D., et al. 2017, ApJ, submitted (arXiv:1711.01314)
Dobbs, M., Bissonnette, E., & Spieler, H. 2008, ITNS, 55, 21
Dobbs, M. A., Lueker, M., Aird, K. A., et al. 2012, RScI, 83, 073113
Galitzki, N., Ade, P. A. R., Angilè, F. E., et al. 2014, Proc. SPIE, 9145, 91450R
Gambrel, A. E. 2018, PhD thesis, Princeton Univ.
Glenn, J., Chattopadhy, G., Edgington, S., et al. 2002, ApOpt, 41, 136
Górski, K. M., Hivon, E., Banday, A. J., et al. 2005, ApJ, 622, 759
Grainger, W., Aboobaker, A. M., Ade, P., et al. 2008, Proc. SPIE, 7020, 70202N
Hanson, D., Hoover, S., Crites, A., et al. 2013, PhRvL, 111, 141301
Hill, C. A., Kusaka, A., Barton, P., et al. 2018, JLTP, tmp, 157
Huber, M. E., Neil, P. A., Benson, R. G., et al. 2001, ITAS, 11, 4048
Hubmayr, J. 2009, PhD thesis, Univ. Minnesota
Hubmayr, J., Aubin, F., Bissonnette, E., et al. 2008, Proc. SPIE, 7020, 70200J
Iida, T., Sakurai, Y., Matsumura, T., et al. 2017, IOP Conference Series: Materials Science and Engineering, 278, 012011
Inoue, Y., Ade, P., Akiba, Y., et al. 2016, Proc. SPIE, 9914, 9914
Jacob, M. V., Mazierska, J., Leong, K., & Krupka, J. 2002, ITMTT, 50, 474
Johnson, B. R., Collins, J., Abroe, M. E., et al. 2007, ApJ, 665, 42
Kes, P. H., Rolfes, J. G. A., & de Klerk, D. 1974, JLTP, 17, 341
Klein, J. 2014, PhD thesis, Univ. Minnesota
Klein, J., Aboobaker, A., Ade, P., et al. 2011, Proc. SPIE, 8150, 815004
Kovac, J. M., Leitch, E. M., Pryke, C., et al. 2002, Natur, 420, 772
Lamb, J. W. 1996, IJIMW, 17, 1997
Lanting, T. M. 2006, PhD thesis, Univ. California, Berkeley
Lee, A. T., Richards, P. L., Nam, S. W., Cabrera, B., & Irwin, K. D. 1996, ApPhL, 69, 1801
Lee, S.-F., Gildemeister, J. M., Holmes, W., Lee, A. T., & Richards, P. L. 1998, ApOpt, 37, 3391
MacDermid, K. 2014, PhD thesis, McGill Univ.
MacDermid, K., Aboobaker, A. M., Ade, P., et al. 2014, Proc. SPIE, 9153, 915311
MacDermid, K., Hyland, P., Aubin, F., et al. 2009, in AIP Conf. Ser. 1185, The 13th International Workshop on Low Temperature Detectors, ed. B. Young, B. Cabrera, & A. Miller (Melville, NY: AIP), 253
Mather, J. C. 1982, ApOpt, 21, 1125
Milligan, M., Ade, P., Aubin, F., et al. 2010, Proc. SPIE, 7740, 774007
Naess, S., Hasselfield, M., McMahon, J., et al. 2014, JCAP, 2014, 007
Oxley, P., Ade, P. A., Baccigalupi, C., et al. 2004, Proc. SPIE, 5543, 320
Planck Collaboration, Adam, R., Ade, P. A. R., et al. 2016, A&A, 594, A10
Polsgrove, D. E. 2009, PhD thesis, Univ. Minnesota
Priestly, M. 1981, Spectral Analysis and Time Series (New York: Academic)
Reichborn-Kjennerud, B. 2010, PhD Thesis, Columbia Univ.
Reichborn-Kjennerud, B., Aboobaker, A. M., Ade, P., et al. 2010, Proc. SPIE, 7741, 77411C
Rownd, B., Bock, J. J., Chattopadhyay, G., et al. 2003, Proc. SPIE, 4855, 510
Sagiv, I., Aboobaker, A. M., Bao, C., et al. 2012, in Twelfth Marcel Grossmann Meeting on General Relativity, ed. A. H. Chamseddine (Singapore: World Scientific Publishing Co.), 2166
Sagiv, I. S. 2011, PhD thesis, Univ. Minnesota
Schwan, D., Ade, P. A. R., Basu, K., et al. 2011, RScI, 82, 091301
Scott, D., & Smoot, G. F. 2010, arXiv:1005.0555

Silva-Feaver, M., Arnold, K., Barron, D., et al. 2018, JLTP, 193, 600
Stebor, N., Ade, P., Akiba, Y., et al. 2016, Proc. SPIE, 9914, 99141H
Suzuki, A., Ade, P. A. R., Akiba, Y., et al. 2018, JLTP, tmp, 124
Suzuki, A. G. 2013, PhD thesis, Univ. California, Berkeley
Takakura, S., Aguilar, M., Akiba, Y., et al. 2017, JCAP, 5, 008
The EBEX Collaboration, Aboobaker, A. M., Ade, P., et al. 2018a, ApJS, 239, 7
The EBEX Collaboration, Aboobaker, A. M., Ade, P., et al. 2018b, ApJS, 239, 9
Van Sciver, S. 2012, Helium Cryogenics (Berlin: Springer)
Weiße, A., Wellein, G., Alvermann, A., & Fehske, H. 2006, RvMP, 78, 275
Westbrook, B., Lee, A., Meng, X., et al. 2012, JLTP, 167, 885
Westbrook, B. G. 2014, PhD thesis, Univ. California
Yoon, J., Clarke, J., Gildemeister, J. M., et al. 2001, ApPhL, 78, 371
Zaldarriaga, M., & Seljak, U. 1997, PhRvD, 55, 1830
Zilic, K. 2014, PhD thesis, Univ. Minnesota